AUT Journal of Electrical Engineering

AUT J. Elec. Eng., 53(2) (2021) 261-286
DOI: 10.22060/eej.2021.19696.5405

Modeling, Small-Signal Stability Analyzing and Implementing of an Inverter-based Distributed Generation with Feed-forwarded Model Predictive Controller

A.H. Saleh

Assistant Professor, Electrical Engineering Department, Malayer University, Malayer, Iran

ABSTRACT: Nowadays the control and stability of DG systems are important topics that researchers in both academia and industry. Small and large signal analyses for stability studies on various systems have been done in papers and books. In this paper, first models of an inverter-based Distributed Generation (DG) subsystems are created. After the linearization, if required, the small-signal stability analysis of the DG which is controlled with a voltage and frequency control scheme based on the model predictive control (MPC) that has been used previously, is established. In this control scheme, load currents at the point of common coupling (PCC) of the DG are considered as disturbances and used as feed-forward signals. This technique enhances the performance of the DG control system in transient and steady-state conditions for a wide range of loads. The stability of the DG system under various loads (such as one phase load as imbalanced load, rectifier load as nonlinear load and induction motor load as dynamic load) is demonstrated by the eigenvalues trajectory. The sensitivity analysis and robustness assessment of the control scheme are also conducted and discussed. For more performance consideration, the DG system is simulated with MATLAB/SIMULINK software, implemented in the lab and later the suitable performance of the system is demonstrated by the simulation and experimental studies.

Review History:
Received: Mar. 03 ,2021
Revised: Jul. 03 ,2021
Accepted: Jul. 04 ,2021
Available Online: Sep. 01, 2021

Keywords:
Small-signal stability
sensitivity analysis
robustness assessment,
distributed generation
model predictive control

1- Introduction

Distributed generations (DGs) offer power plants that use micro-sources as main energy producer. Micro-sources are consisted of DC sources such as photovoltaic arrays and AC sources such as wind turbines, where two types of them are non-dispatchable sources, and micro-turbines and fuel cells are dispatchable sources [1]. Loads in the DG system can be divided into four main clusters: 1) three-phase balanced load 2) unbalanced load 3) three-phase induction motor load 4) three-phase rectifier load [2]. DGs operate in grid-connected and islanded modes, where the islanded operating mode must provide loads demanded power in addition to regulation of voltage magnitude and frequency [3]. Various control schemes have been proposed in previous papers [4-8, 28]. Therefore, the control schemes consist of nested control loops and the performance of DG systems is affected by the control schemes under the mentioned load categories. The control and stability of the DG systems are important topics that researchers in both academia and industry have been addressing [9]. Small and large signal analysis for stability studies on various systems have been done in papers and books [10-13]. Stability analysis validation of a system is depended on validation of the mathematic model of the subsystems of it [14]. Nonlinear equations are suitable for large-signal analysis and simulation studies. It cannot readily be understood from the nonlinear equations as to how each dynamic mode is influenced by different parameters. Therefore, the nonlinear equations are linearized about a system steady-state operating point, to provide a linear model and small-signal analyses are conducted. Linear analysis tools such as eigenvalue and sensitivity analysis are used to study these linearized systems [12]. Based on these linear analyses the influences of various parameters on the system performance can be studied. Therefore, the operation of the system under study can promote by setting the effective parameters. Thus, the small-signal analysis has this superiority which large-signal analysis lack. The power outputs of wind turbines, photovoltaic arrays and other renewable sources are time-variant, which can be regarded as small disturbances. They may couple with load fluctuations too. Thus, these kinds of small power fluctuations are so frequent that they affect the operation status of DG systems constantly. The difficulty and necessity of study of small-signal stability of DG units is evident [25]. Small-signal models for rectifiers [11], motors [12], synchronous and induction generators [15] and inverters [16] have been presented for Micro-Grid (MG) applications [17]. However, the derived linear model is valid only for small perturbations of the system around the

*Corresponding author's email: hosein.saleh@chmail.ir

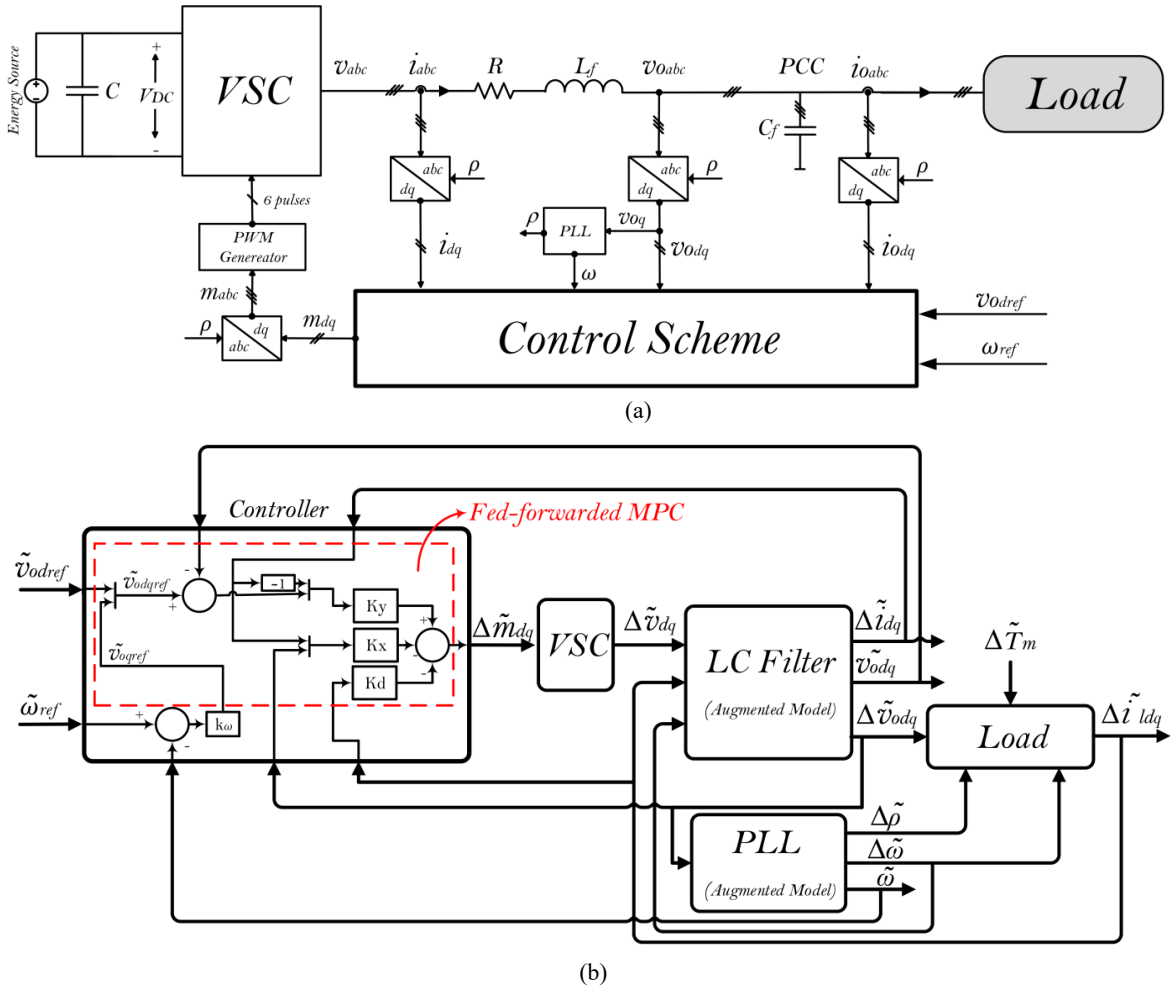

Fig. 1. (a) The schematic diagram of the DG system [4] (b) The block diagram of difference of small-signal model of the DG system.

operating point [18].

This paper focuses on the small signal stability analysis of a DG unit system which is controlled by a voltage and frequency control scheme based on model predictive control (MPC) which presented in [4] where currents drown with the load at the point of common coupling (PCC) of the DG are considered as disturbances and used as feed-forward signals. This technique which has been used in [4] enhances the performance of the DG control system in transient and steady-state conditions for a wide range of loads. In this paper, a detailed model of the unbalanced, rectifier loads and MPC are established that were not presented previously, and finally the overall small-signal model of the DG system established and several linear analyses are presented to investigate stability of the system under various conditions. In [4] the stability and robustness analyses have been established based on Lyapunov function method while cannot be understood how each dynamic mode is influenced by different parameters (i.e. sensitivity analysis). The proposed modal analysis can be used in future studies that consider MGs which consist of several DGs [19-20, 26-27]. The proposed complicated control scheme which presented in [4] is also implemented in laboratory environment and the advantages of the proposed scheme are demonstrated based on the results.

The rest of the paper is divided as follows. Section II explains DG unit and its main controller. Section III presents mathematic models of subsystems of the DG system. In section IV represents simulation studies and in section V stability and sensitivity analysis and robustness assessment have been performed. Experimental studies are presented in section VI, and finally, the conclusions are drawn in Section VII.

2- DG and Its Main Controller

A typical inverter-based DG and its main controller which is based on discrete-time MPC and proposed in [4], are shown in Fig. 1(a). PCC voltage magnitude ($|v_o| = \sqrt{v_{od}^2 + v_{oq}^2}$) and frequency (ω) are regulated with main controller at their

given references are regulated with the main controller. When the PLL tracks the phase angle accurately, $v_{oq}=0$, thus $|v_o|=v_{od}$ and the regulation of the PCC voltage magnitude can be changed into the regulation of v_{od} (i.e. $v_{odref}=v_{oref}$). Based on [3] and [21], frequency is controlled using v_{oq} so that $v_{oqref}=k_\omega(\omega_{ref}-\omega)$. The coefficient k_ω is a simple gain.

The differences of the state-space, output equations and the control scheme in synchronous dq reference frame are given in [4]. In the next section, mathematic models of DG subsystems (micro-source, inverter, LC filter, controllers, PLL and loads) are established based on [4] with aims of small-signal stability analysis. Since the controller in [4] has been designed based on difference of discrete-time state-space model of the system, the difference of discrete-time mathematic model of these subsystems will be established.

3- Mathematic Models

The block diagram of difference of small-signal model of DG system shown in Fig. 1(b). Relation between blocks is based on their inputs and outputs.

3-1- Micro-Source Model

Micro-sources are consisted of DC sources such as photovoltaic arrays (non-dispatchable), AC sources such as wind turbines (non-dispatchable) and micro-turbines (dispatchable). In DC sources, the DC voltage is changed to AC with inverter. In AC sources first the AC voltage is changed to DC with rectifier, and later the DC voltage changed to AC with an inverter in standard frequency (50 or 60 Hz). Thus, all the non-dispatchable micro-sources are usually connected to an inverter that are equipped with an energy storage at DC-side. Therefore, the slow dynamic of those micro-sources is not affected by the fast dynamic of the AC-side of the inverter and the dynamics of them are decoupled. Therefore, a micro-source can be modeled with an ideal fixed DC voltage source V_{DC} .

3-2- Inverter Model

The average model for inverter is chosen and switching is neglected. Thus, in dq reference frame [22]:

$$v_{dq}=m_{dq}*\frac{V_{DC}}{2} \tag{1}$$

m_{dq} are dq components of modulating indexes and are produced by controller. This model is linear, thus the difference of its discrete-time linearized model is as (2) [23].

$$\Delta\tilde{v}_{dq}(k)=\Delta\tilde{m}_{dq}(k)*\frac{V_{DC}}{2} \tag{2}$$

3-3- LC Filter Model

Based on Fig. 1(a) and [24], the mathematic model of LC filter in dq reference frame is:

$$\begin{aligned}
\frac{d(i_d)}{dt}&=\omega i_q-\frac{R_f}{L_f}i_d+\frac{1}{L_f}(v_d-v_{od})\\
\frac{d(i_q)}{dt}&=-\omega i_d-\frac{R_f}{L_f}i_q+\frac{1}{L_f}(v_q-v_{oq})\\
\frac{d(v_{od})}{dt}&=\omega v_{oq}+\frac{1}{C_f}(i_d-i_{od})\\
\frac{d(v_{oq})}{dt}&=-\omega v_{od}+\frac{1}{C_f}(i_q-i_{oq})
\end{aligned} \tag{3}$$

Since PLL processes v_{oq} and then produces ω, the above equations are nonlinear. They are later linearized and the state-space and output equations of LC filter are as below:

$$\begin{aligned}
&\left[\dot{\tilde{x}}_{LC}\right]=Ac_{LC}\left[\tilde{x}_{LC}\right]+B1c_{LC}\left[\tilde{v}_{dq}\right]+\\
&B2c_{LC}\tilde{\omega}+B3c_{LC}\left[\tilde{i}_{ldq}\right]\\
&\left[\tilde{v}_{odq}\right]=Cc_{LC}\left[\tilde{x}_{LC}\right],\ \left[\tilde{x}_{LC}\right]=\begin{bmatrix}\tilde{i}_{dq}\\ \tilde{v}_{odq}\end{bmatrix}.\\
&Ac_{LC}=\begin{bmatrix}-\frac{R_f}{L_f} & \omega_0 & -\frac{1}{L_f} & 0\\ -\omega_0 & -\frac{R_f}{L_f} & 0 & -\frac{1}{L_f}\\ \frac{1}{C_f} & 0 & 0 & \omega_0\\ 0 & \frac{1}{C_f} & -\omega_0 & 0\end{bmatrix}.
\end{aligned} \tag{4}$$

$$B1'c_{LC}=\begin{bmatrix}\frac{1}{L_f} & 0\\ 0 & \frac{1}{L_f}\\ 0 & 0\\ 0 & 0\end{bmatrix}.\quad B2c_{LC}=\begin{bmatrix}I_{q0}\\ -I_{d0}\\ V_{oq0}\\ -V_{od0}\end{bmatrix}.$$

$$B3c_{LC}=\begin{bmatrix}0 & 0\\ 0 & 0\\ -\frac{1}{C_f} & 0\\ 0 & -\frac{1}{C_f}\end{bmatrix}.Cc_{LC}=\begin{bmatrix}0 & 0 & 1 & 0\\ 0 & 0 & 0 & 1\end{bmatrix}$$

The linearized model is the function of steady-state operation point. Due to (2), the difference of discrete-time linearized model [23] of LC filter and inverter, will be as (5).

$$\begin{aligned}&\left[\Delta\tilde{\boldsymbol{x}}_{mLC}(k+1)\right]=Am_{LC}\left[\Delta\tilde{\boldsymbol{x}}_{mLC}(k)\right]+B1m_{LC}\left[\Delta\tilde{m}_{dq}(k)\right]+\\ &B2m_{LC}\Delta\tilde{\omega}(k)+B3m_{LC}\left[\Delta\tilde{i}_{ldq}(k)\right]\\ &\left[\Delta\tilde{v}_{odq}(k)\right]=Cm_{LC}\left[\Delta\tilde{\boldsymbol{x}}_{mLC}(k)\right]\end{aligned}\tag{5}$$

$\Delta\tilde{m}_{dq}$ are produced by the controller. $\Delta\tilde{i}_{ldq}$ and $\Delta\tilde{\omega}$ are from the load and PL. The augmented model of the LC filter that must consist of small-signal of v_{odq} and the difference of small-signal will be required. Thus, based on the equation $f(k+1)=\Delta f(k+1)+f(k)$, augmented model [23] of LC filter is established as (6).

$$\begin{aligned}&\begin{bmatrix}\Delta\tilde{\boldsymbol{x}}_{mLC}(k+1)\\ \tilde{v}_{odq}(k+1)\end{bmatrix}=\begin{bmatrix}Am_{LC} & 0\\ Cm_{LC}Am_{LC} & I_{2\times2}\end{bmatrix}\begin{bmatrix}\Delta\tilde{\boldsymbol{x}}_{mLC}(k)\\ \tilde{v}_{odq}(k)\end{bmatrix}\\ &+\begin{bmatrix}B1m_{LC}\\ Cm_{LC}B1m_{LC}\end{bmatrix}\left[\Delta\tilde{m}_{dq}(k)\right]+\begin{bmatrix}B2m_{LC}\\ Cm_{LC}B2m_{LC}\end{bmatrix}\Delta\tilde{\omega}(k)\\ &+\begin{bmatrix}B3m_{LC}\\ Cm_{LC}B3m_{LC}\end{bmatrix}\left[\Delta\tilde{i}_{ldq}(k)\right].\end{aligned}\tag{6}$$

3-4- Controllers Model

3-4-1- Voltage Controller Based on MPC

Based on [4],

$$\begin{aligned}&\left[\Delta\tilde{m}_{dq}(k)\right]=K_{y\,2\times4}\begin{bmatrix}\tilde{i}_{dqref}(k)-\tilde{i}_{dq}(k)\\ \tilde{v}_{odqref}(k)-\tilde{v}_{odq}(k)\end{bmatrix}\\ &-K_{x\,2\times4}\begin{bmatrix}\Delta\tilde{i}_{dq}(k)\\ \Delta\tilde{v}_{odq}(k)\end{bmatrix}-K_{d\,2\times2}\left[\Delta\tilde{i}_{ldq}(k)\right]\end{aligned}\tag{7}$$

where $\tilde{i}_{dqref}(k)=\tilde{i}_{dq}(k-1)$, thus:

$$\begin{aligned}&\left[\Delta\tilde{m}_{dq}(k)\right]=K_{y\,2\times4}\begin{bmatrix}\tilde{i}_{dq}(k-1)-\tilde{i}_{dq}(k)\\ \tilde{v}_{odqref}(k)-\tilde{v}_{odq}(k)\end{bmatrix}\\ &-K_{x\,2\times4}\begin{bmatrix}\Delta\tilde{i}_{dq}(k)\\ \Delta\tilde{v}_{odq}(k)\end{bmatrix}-K_{d\,2\times2}\left[\Delta\tilde{i}_{ldq}(k)\right]\\ &=K_{y\,2\times4}\begin{bmatrix}-\Delta\tilde{i}_{dq}(k)\\ \tilde{v}_{odqref}(k)-\tilde{v}_{odq}(k)\end{bmatrix}-K_{x\,2\times4}\begin{bmatrix}\Delta\tilde{i}_{dq}(k)\\ \Delta\tilde{v}_{odq}(k)\end{bmatrix}\\ &-K_{d\,2\times2}\left[\Delta\tilde{i}_{ldq}(k)\right]=\end{aligned}$$

$$\underbrace{\begin{bmatrix}K_{yi} & K_{yv}\end{bmatrix}}_{K_{y\,2\times4}}\begin{bmatrix}-\Delta\tilde{i}_{dq}(k)\\ \tilde{v}_{odqref}(k)-\tilde{v}_{odq}(k)\end{bmatrix}-$$

$$\underbrace{\begin{bmatrix}K_{xi} & K_{xv}\end{bmatrix}}_{K_{x\,2\times4}}\begin{bmatrix}\Delta\tilde{i}_{dq}(k)\\ \Delta\tilde{v}_{odq}(k)\end{bmatrix}-K_{d\,2\times2}\left[\Delta\tilde{i}_{ldq}(k)\right]=\tag{8}$$

$$K_{yv}\left[\tilde{v}_{odqref}(k)\right]-K_{yv}\left[\tilde{v}_{odq}(k)\right]-$$

$$\underbrace{\begin{bmatrix}K_{xi}+K_{yi} & K_{xv}\end{bmatrix}}_{K}\begin{bmatrix}\Delta\tilde{i}_{dq}(k)\\ \Delta\tilde{v}_{odq}(k)\end{bmatrix}-K_d\left[\Delta\tilde{i}_{ldq}(k)\right]$$

3-4-2- Frequency controller

As [4] follows:

$$v_{oqref}=K_{\omega}(\omega_{ref}-\omega)\tag{9}$$

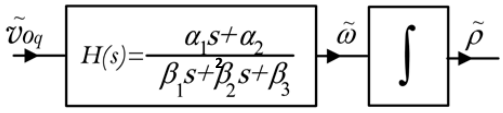

Fig. 2. Block diagram of linearized PLL

Since this equation is linear the discrete-time linearized model of it is:

$$\tilde{v}_{oqref}(k)=K_{\omega}\left(\tilde{\omega}_{ref}(k)-\tilde{\omega}(k)\right) \tag{10}$$

By substituting (10) in (8) the output of the controller is:

$$\left[\Delta\tilde{m}_{dq}(k)\right]=\left[\underbrace{K_{yvd}\ \vdots\ K_{yvq}}_{K_{yv}}K_{\omega}\right]\begin{bmatrix}\tilde{v}_{odref}(k)\\ \tilde{\omega}_{ref}(k)\end{bmatrix}-$$

$$K_{yvq}K_{\omega}\tilde{\omega}(k)-K_{yv}\left[\tilde{v}_{odq}(k)\right]- \tag{11}$$

$$\underbrace{\begin{bmatrix}K_{xi}+K_{yi} & K_{xv}\end{bmatrix}}_{K}\begin{bmatrix}\Delta\tilde{i}_{dq}(k)\\ \Delta\tilde{v}_{odq}(k)\end{bmatrix}-K_d\left[\Delta\tilde{i}_{ldq}(k)\right].$$

$\tilde{v}_{odq}$, $\Delta\tilde{v}_{odq}$ and $\Delta\tilde{i}_{dq}$ must come from the LC filter. Since the mathematic model of LC filter must consist of small-signal of v_{odq} and the difference of small-signal, the augmented model of LC filter is required which is given in (6). $\tilde{\omega}$ must be produced by PLL, and $\Delta\tilde{i}_{ldq}$ are from load model. Additionally, $\tilde{v}_{odref}$ and $\tilde{\omega}_{ref}$ are small signals of the references.

3-5- PLL Model

The block diagram of linearized PLL is shown in Fig. 2.

The state-space and output equations of PLL are [2]:

$$\left[\dot{\tilde{x}}_{PLL}\right]=Ac_{PLL}\left[\tilde{x}_{PLL}\right]+Bc_{PLL}\left[\tilde{v}_{odq}\right]\ ;\ \left[\tilde{x}_{PLL}\right]=\begin{bmatrix}\tilde{x}_{1PLL}\\ \tilde{x}_{2PLL}\\ \tilde{\rho}\end{bmatrix}$$

$$\left[\tilde{\omega}\right]=C\omega c_{PLL}\left[\tilde{x}_{PLL}\right],\ \left[\tilde{\rho}\right]=C\rho c_{PLL}\left[\tilde{x}_{PLL}\right], \tag{12}$$

$$Ac_{PLL}=\begin{bmatrix}-\frac{\beta_2}{\beta_1} & -\frac{\beta_3}{\beta_1} & 0\\ 1 & 0 & 0\\ \frac{\alpha_1}{\beta_1} & \frac{\alpha_2}{\beta_1} & 0\end{bmatrix}.Bc_{PLL}=\begin{bmatrix}0 & 1\\ 0 & 0\\ 0 & 0\end{bmatrix},$$

$$C\omega c_{PLL}=\begin{bmatrix}\frac{\alpha_1}{\beta_1} & \frac{\alpha_2}{\beta_1} & 0\end{bmatrix}.\ C\rho c_{PLL}=\begin{bmatrix}0 & 0 & 1\end{bmatrix}$$

Thus, the difference of small-signal model of PLL is as (13).

$$\begin{aligned}\left[\Delta\tilde{x}_{mPLL}(k+1)\right]&=Am_{PLL}\left[\Delta\tilde{x}_{mPLL}(k)\right]+Bm_{PLL}\left[\Delta\tilde{v}_{odq}(k)\right]\\ \left[\Delta\tilde{\omega}(k)\right]&=C\omega m_{PLL}\left[\Delta\tilde{x}_{mPLL}(k)\right]\\ \left[\Delta\tilde{\rho}(k)\right]&=C\rho m_{PLL}\left[\Delta\tilde{x}_{mPLL}(k)\right]\end{aligned} \tag{13}$$

Based on (5) and (11), PLL must produce $\tilde{\omega}$ in addition to $\Delta\tilde{\omega}$ and $\Delta\tilde{\rho}$. Thus, (13) is augmented and:

$$\begin{bmatrix}\Delta\tilde{x}_{mPLL}(k+1)\\ \tilde{\omega}(k+1)\end{bmatrix}=\begin{bmatrix}Am_{PLL} & 0\\ C\omega m_{PLL}Am_{PLL} & 1\end{bmatrix}\begin{bmatrix}\Delta\tilde{x}_{mPLL}(k)\\ \tilde{\omega}(k)\end{bmatrix}$$

$$+\begin{bmatrix}Bm_{PLL}\\ C\omega m_{PLL}Bm_{PLL}\end{bmatrix}\left[\Delta\tilde{v}_{odq}(k)\right] \tag{14}$$

where $\Delta\tilde{v}_{odq}$, are from LC filter.

3-6- Loads Models

Four types of loads are considered:

1) three-phase balanced RL load

2) one-phase RL load which is connected to the secondary winding of Δ/Y three-phase transformer as an unbalanced load

3) three-phase induction motor load

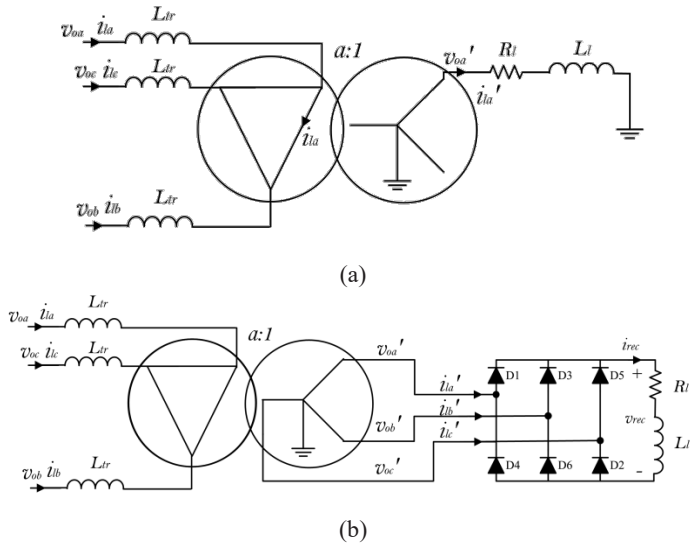

Fig. 3. The schematic diagrams of the considered loads: (a) One-phase RL load connected to secondary winding of Δ/Y three-phase transformer as an unbalanced load (b) rectifier load connected to secondary winding of Δ/Y three-phase transformer as a nonlinear load.

4) rectifier load which is connected to the secondary winding of Δ/Y three-phase transformer as a nonlinear load.

Their schematic diagrams are shown in Fig. 3. First the linearized model of the loads, and then their difference in a general case are established. In all load models, input and output variables are v_{odq} and i_{ldq}. It is assumed that the initial current is very lower than the rated current and the parallel branch in their electrical model are neglected for power transformers.

3-6-1- Three-phase Balanced RL Load

This load's mathematic model has been presented in published papers. Note that its state variables are i_{ldq}, which must be the outputs of the load model and are LC filter inputs.

3-6-2- One-phase RL Load Connected to the Secondary Winding of Dy11 Three-phase Transformer as an Unbalanced Load

Fig. 3(a) shows this load. Its mathematic model is:

$$\frac{d\left(i_{la}\right)}{dt}=-\frac{R_l'}{L_l'+2L_{tr}}i_{la}+\frac{1}{L_l'+2L_{tr}}\left(v_{oa}-v_{ob}\right)$$
$$\frac{d\left(i_{lb}\right)}{dt}=-\frac{R_l'}{L_l'+2L_{tr}}i_{lb}+\frac{1}{L_l'+2L_{tr}}\left(v_{ob}-v_{oa}\right) \quad (15)$$
$$R_l^{'}=\left(a\sqrt{3}\right)^2 R_l \quad . \quad L_l^{'}=\left(a\sqrt{3}\right)^2 L_l$$

Above equations rewritten as (16).

$$\frac{d}{dt}\begin{bmatrix} i_{la} \\ i_{lb} \end{bmatrix}=\begin{bmatrix} -\frac{R_l'}{L_l'+2L_{tr}} & 0 \\ 0 & -\frac{R_l'}{L_l'+2L_{tr}} \end{bmatrix}\begin{bmatrix} i_{la} \\ i_{lb} \end{bmatrix} \quad (16)$$
$$+\frac{1}{L_l'+2L_{tr}}\begin{bmatrix} 1 & -1 \\ -1 & 1 \end{bmatrix}\begin{bmatrix} v_{oa} \\ v_{ob} \end{bmatrix}$$

By substituting $\begin{bmatrix} i_{la} \\ i_{lb} \end{bmatrix}$ with $T_{ab}\begin{bmatrix} i_{ld} \\ i_{lq} \end{bmatrix}$ and $\begin{bmatrix} v_{oa} \\ v_{ob} \end{bmatrix}$ with $T_{ab}\begin{bmatrix} v_{od} \\ v_{oq} \end{bmatrix}$ where $T_{ab}=\begin{bmatrix} \sin(\rho) & \cos(\rho) \\ \sin(\rho-2\pi/3) & \cos(\rho-2\pi/3) \end{bmatrix}$:

For the left-side of (17):

$$\frac{d}{dt}\left(T_{ab}\begin{bmatrix} i_{ld} \\ i_{lq} \end{bmatrix}\right)=\begin{bmatrix} -\frac{R_l'}{L_l'+2L_{tr}} & 0 \\ 0 & -\frac{R_l'}{L_l'+2L_{tr}} \end{bmatrix}T_{ab}\begin{bmatrix} i_{ld} \\ i_{lq} \end{bmatrix} \quad (17)$$
$$+\frac{1}{L_l'+2L_{tr}}\begin{bmatrix} 1 & -1 \\ -1 & 1 \end{bmatrix}T_{ab}\begin{bmatrix} v_{od} \\ v_{oq} \end{bmatrix}.$$

$$\frac{d}{dt}\left(T_{ab}\begin{bmatrix} i_{ld} \\ i_{lq} \end{bmatrix}\right)=T_{ab}\frac{d}{dt}\left(\begin{bmatrix} i_{ld} \\ i_{lq} \end{bmatrix}\right)+\frac{d}{dt}\left(T_{ab}\right)\begin{bmatrix} i_{ld} \\ i_{lq} \end{bmatrix} \quad (18)$$

From (17) and (18) concluded that:

$$\frac{d}{dt}\begin{bmatrix} i_{ld} \\ i_{lq} \end{bmatrix} = \left(T_{ab}^{-1} \begin{bmatrix} -\dfrac{R_l'}{L_l'+2L_{tr}} & 0 \\ 0 & -\dfrac{R_l'}{L_l'+2L_{tr}} \end{bmatrix} T_{ab} + T_{ab}^{-1} \frac{d}{dt}\left(T_{ab}\right) \right) \begin{bmatrix} i_{ld} \\ i_{lq} \end{bmatrix} + \frac{1}{L_l'+2L_{tr}} T_{ab}^{-1} \begin{bmatrix} 1 & -1 \\ -1 & 1 \end{bmatrix} T_{ab} \begin{bmatrix} v_{od} \\ v_{oq} \end{bmatrix} \quad (19)$$

where $T_{ab}^{-1} = \frac{2}{\sqrt{3}} \begin{bmatrix} \cos(\rho - 2\pi/3) & -\cos(\rho) \\ -\sin(\rho - 2\pi/3) & \sin(\rho) \end{bmatrix}$. After simplifications, (20) is deduced.

$$\frac{d}{dt}\begin{bmatrix} i_{ld} \\ i_{lq} \end{bmatrix} = \begin{bmatrix} -\dfrac{R_l'}{L_l'+2L_{tr}} & \omega \\ -\omega & -\dfrac{R_l'}{L_l'+2L_{tr}} \end{bmatrix} \begin{bmatrix} i_{ld} \\ i_{lq} \end{bmatrix} \frac{2}{\sqrt{3}} \frac{1}{L_l'+2L_{tr}} \cdot \begin{bmatrix} \frac{\sqrt{3}}{2} - \frac{1}{2}\sin\left(2\rho - \frac{4\pi}{3}\right) + \frac{1}{2}\sin(2\rho) & -cos^2\left(\rho - \frac{2\pi}{3}\right) + cos^2(\rho) \\ sin^2\left(\rho - \frac{2\pi}{3}\right) - sin^2(\rho) & \frac{\sqrt{3}}{2} + \frac{1}{2}\sin\left(2\rho - \frac{4\pi}{3}\right) - \frac{1}{2}\sin(2\rho) \end{bmatrix} \begin{bmatrix} v_{od} \\ v_{oq} \end{bmatrix} \quad (20)$$

These equations are nonlinear. Thus they are linearized and the state-space and output equations will be as (21).

$$\begin{aligned} \left[\dot{\tilde{\boldsymbol{x}}}_{load}\right] &= Ac_{load}\left[\tilde{\boldsymbol{x}}_{load}\right] + B1c_{load}\left[\tilde{v}_{odq}\right] \\ &+ B2c_{load}\tilde{\omega} + B3c_{load}\tilde{\rho}, \\ \left[\tilde{i}_{ldq}\right] &= Cc_{load}\left[\tilde{\boldsymbol{x}}_{load}\right] \quad , \quad \left[\tilde{\boldsymbol{x}}_{load}\right] = \left[\int \tilde{i}_{ldq}\right] \\ Ac_{load} &= \begin{bmatrix} -\dfrac{R_l'}{L_l'+2L_{tr}} & \omega_0 \\ -\omega_0 & -\dfrac{R_l'}{L_l'+2L_{tr}} \end{bmatrix} \end{aligned} \quad (21)$$

$$B1c_{load} = \frac{2}{\sqrt{3}} \frac{1}{L_l' + 2L_{tr}} \begin{bmatrix} \frac{\sqrt{3}}{2} - \frac{1}{2}sin\left(2\rho_0 - \frac{4\pi}{3}\right) + \frac{1}{2}sin(2\rho_0) \\ sin^2\left(\rho_0 - \frac{2\pi}{3}\right) - sin^2(\rho_0) \\ -cos^2\left(\rho_0 - \frac{2\pi}{3}\right) + cos^2(\rho_0) \\ \frac{\sqrt{3}}{2} + \frac{1}{2}sin\left(2\rho_0 - \frac{4\pi}{3}\right) - \frac{1}{2}sin(2\rho_0) \end{bmatrix}.$$

$$B2c_{load} = \begin{bmatrix} I_{lq0} \\ -I_{ld0} \end{bmatrix},$$

$$B3c_{load} = \frac{2}{\sqrt{3}} \frac{1}{L_l' + 2L_{tr}} \begin{bmatrix} -cos\left(2\rho_0 - \frac{4\pi}{3}\right) + cos(2\rho_0) & sin\left(2\rho_0 - \frac{4\pi}{3}\right) - sin(2\rho_0) \\ sin\left(2\rho_0 - \frac{4\pi}{3}\right) - sin(2\rho_0) & cos\left(2\rho_0 - \frac{4\pi}{3}\right) - cos(2\rho_0) \end{bmatrix} [V_{odq0}]$$

$$Cc_{load} = \begin{bmatrix} 1 & 0 \\ 0 & 1 \end{bmatrix}$$

3-6-3- Three-phase Induction Motor Load

The mathematic model of the three-phase induction motor has been established in [15]. This model has five state variables $\boldsymbol{x}_{motor\ load} = \left[\psi_{sdq} \quad \psi_{rdq} \quad \omega_r\right]^T$. ψ_{sdq} and ψ_{rdq} are dq components of linkage fluxes of stator and rotor. The output variables are i_{ldq}, which are the stator currents. Inputs of this model are v_{odq} and T_m.

3-6-4- Full Bridge Rectifier Load Connected to the Secondary Winding of Dy11 Three-phase Transformer as a Nonlinear Load

Fig. 3(b) shows this load. Suppose that v_{oabc} is as (22).

$$v_{oabc}(t) = \begin{bmatrix} v_m \sin(\omega t) \\ v_m \sin\left(\omega t - \frac{2\pi}{3}\right) \\ v_m \sin\left(\omega t - \frac{4\pi}{3}\right) \end{bmatrix} = \begin{bmatrix} v_m \sin(\rho) \\ v_m \sin\left(\rho - \frac{2\pi}{3}\right) \\ v_m \sin\left(\rho - \frac{4\pi}{3}\right) \end{bmatrix} \quad (22)$$

Since the line to line voltage phase of delta-side is 30 degrees smaller than the star-side of the transformer, the phasor diagram of the voltages is as Fig. 4. Due to Fig. 3(b) and Fig.4, simplified equivalent circuits of the variety of intervals of ρ are shown in Table1. For $0 < \rho < \frac{\pi}{3}$, due to its equivalent circuit and symmetry, half of the load is transferred to the primary side between a and b nodes and the other half

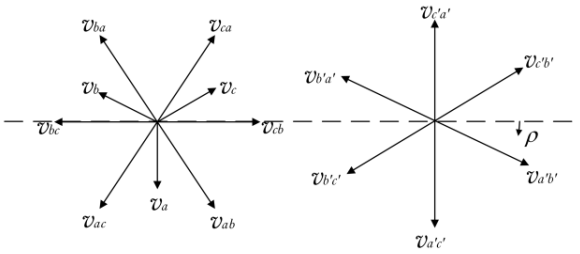

Fig. 4. Voltages phasor diagram

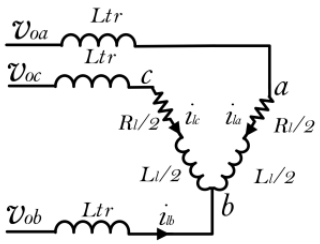

Fig. 5. New equivalent circuit for 0<ρ<π/3

Table 1. Simplified equivalent circuits of nonlinear load in ρ intervals

$0 < \rho < \frac{\pi}{3}$	Maximum L-L voltage = $v_{oa'b'} = v_{rec}$ On-state diodes: *D1* , *D6* Simplified equivalent circuit:	$\frac{\pi}{3} < \rho < \frac{2\pi}{3}$	Maximum L-L voltage = $v_{oa'c'} = v_{rec}$ On-state diodes: *D1* , *D2* Simplified equivalent circuit:
$\frac{2\pi}{3} < \rho < \pi$	Maximum L-L voltage = $v_{ob'c'} = v_{rec}$ On-state diodes: *D2* , *D3* Simplified equivalent circuit:	$\pi < \rho < \frac{4\pi}{3}$	Maximum L-L voltage = $v_{ob'a'} = v_{rec}$ On-state diodes: *D3*, *D4* Simplified equivalent circuit:
$\frac{4\pi}{3} < \rho < \frac{5\pi}{3}$	Maximum L-L voltage = $v_{oc'a'} = v_{rec}$ On-state diodes: *D4*, *D5* Simplified equivalent circuit:	$\frac{5\pi}{3} < \rho < 2\pi$	Maximum L-L voltage = $v_{oc'b'} = v_{rec}$ On-state diodes: *D5*, *D6* Simplified equivalent circuit:

between c and b nodes. New equivalent circuit is produced as Fig. 5. Thus, KVL can be written between a and b nodes as:

$$\frac{d\left(i_{la}\right)}{dt} = -\frac{R_l'}{L_l'+6L_{tr}} i_{la} + \frac{2}{L_l'+6L_{tr}}\left(v_{oa} - v_{ob}\right) \qquad (23)$$

$$R_l' = \left(a\sqrt{3}\right)^2 R_l \quad . \quad L_l' = \left(a\sqrt{3}\right)^2 L_l$$

According to Fig. 4, by substituting i_{la} with i_{lc} or $-\frac{i_{lb}}{2}$ in (23), (24) is deduced:

$$\frac{d\left(i_{lb}\right)}{dt} = -\frac{R_l'}{L_l'+6L_{tr}} i_{lb} + \frac{2}{L_l'+6L_{tr}}\left(2v_{ob} - 2v_{oa}\right)$$
$$\frac{d\left(i_{lc}\right)}{dt} = -\frac{R_l'}{L_l'+6L_{tr}} i_{lc} + \frac{2}{L_l'+6L_{tr}}\left(v_{oa} - v_{ob}\right) \qquad (24)$$

Thus, state-space equations of this ρ interval will be as (25).

$$\frac{d}{dt}\begin{bmatrix} i_{la} \\ i_{lb} \\ i_{lc} \end{bmatrix} = \begin{bmatrix} -\frac{R_l'}{L_l'+6L_{tr}} & 0 & 0 \\ 0 & -\frac{R_l'}{L_l'+6L_{tr}} & 0 \\ 0 & 0 & -\frac{R_l'}{L_l'+6L_{tr}} \end{bmatrix} \begin{bmatrix} i_{la} \\ i_{lb} \\ i_{lc} \end{bmatrix} + \frac{2}{L_l'+6L_{tr}} \begin{bmatrix} 1 & -1 & 0 \\ -2 & 2 & 0 \\ 1 & -1 & 0 \end{bmatrix} \begin{bmatrix} v_{oa} \\ v_{ob} \\ v_{oc} \end{bmatrix} \quad (25)$$

(39) transferred to dq frame as (26).

$$\frac{d}{dt}\left[i_{ldq}\right] = \begin{bmatrix} -\frac{R_l'}{L_l'+6L_{tr}} & \omega_0 \\ -\omega_0 & -\frac{R_l'}{L_l'+6L_{tr}} \end{bmatrix} \left[i_{ldq}\right] + \frac{2}{L_l'+6L_{tr}} T \begin{bmatrix} 1 & -1 & 0 \\ -2 & 2 & 0 \\ 1 & -1 & 0 \end{bmatrix} T^{-1} \left[v_{odq}\right] \quad (26)$$

Where $T = \frac{2}{3}\begin{bmatrix} sin(\rho) & sin(\rho-2\pi/3) & sin(\rho-4\pi/3) \\ cos(\rho) & cos(\rho-2\pi/3) & cos(\rho-4\pi/3) \end{bmatrix}$

and $T^{-1} = \begin{bmatrix} sin(\rho) & cos(\rho) \\ sin(\rho-2\pi/3) & cos(\rho-2\pi/3) \\ sin(\rho-4\pi/3) & cos(\rho-4\pi/3) \end{bmatrix}$.

For $\frac{\pi}{3} < \rho < \frac{2\pi}{3}$, with respect to its equivalent circuit and symmetry, such as the established analysis for $0 < \rho < \frac{\pi}{3}$, the state-space equations in dq frame will be:

$$\frac{d}{dt}\left[i_{ldq}\right] = \begin{bmatrix} -\frac{R_l'}{L_l'+6L_{tr}} & \omega_0 \\ -\omega_0 & -\frac{R_l'}{L_l'+6L_{tr}} \end{bmatrix} \left[i_{ldq}\right] + \frac{2}{L_l'+6L_{tr}} T \begin{bmatrix} 2 & 0 & -2 \\ -1 & 0 & 1 \\ -1 & 0 & 1 \end{bmatrix} T^{-1} \left[v_{odq}\right] \quad (27)$$

And for $\frac{2\pi}{3} < \rho < \pi$:

$$\frac{d}{dt}\left[i_{ldq}\right] = \begin{bmatrix} -\frac{R_l'}{L_l'+6L_{tr}} & \omega_0 \\ -\omega_0 & -\frac{R_l'}{L_l'+6L_{tr}} \end{bmatrix} \left[i_{ldq}\right] + \frac{2}{L_l'+6L_{tr}} T \begin{bmatrix} 2 & 0 & -2 \\ -1 & 0 & 1 \\ -1 & 0 & 1 \end{bmatrix} T^{-1} \left[v_{odq}\right] \quad (28)$$

The state-space equations for $< \rho < \frac{4\pi}{3}$, $\frac{4\pi}{3} < \rho < \frac{5\pi}{3}$ and $\frac{5\pi}{3} < \rho < 2\pi$ are as same as $0 < \rho < \frac{\pi}{3}$, $\frac{\pi}{3} < \rho < \frac{2\pi}{3}$ and $\frac{2\pi}{3} < \rho < \pi$. Equations (26) - (28) are nonlinear. Thus, they are linearized [2] and the state-space and output equations will be as (29).

$$\left[\dot{\tilde{\boldsymbol{x}}}_{load}\right] = Ac_{load}\left[\tilde{\boldsymbol{x}}_{load}\right] + B1c_{load}\left[\tilde{v}_{odq}\right] + B2c_{load}\tilde{\omega} + B3c_{load}\tilde{\rho}$$

$$\left[\tilde{i}_{ldq}\right] = Cc_{load}\left[\tilde{\boldsymbol{x}}_{load}\right], \left[\tilde{\boldsymbol{x}}_{load}\right] = \left[\tilde{i}_{ldq}\right],$$

$$Ac_{load} = \begin{bmatrix} -\frac{R_l'}{L_l'+6L_{tr}} & \omega_0 \\ -\omega_0 & -\frac{R_l'}{L_l'+6L_{tr}} \end{bmatrix}, Cc_{load} = \begin{bmatrix} 1 & 0 \\ 0 & 1 \end{bmatrix}$$

$$B1c_{load} = \frac{2}{L_l'+6L_{tr}}\frac{2}{3} * \begin{bmatrix} \sin(\rho_0) & \sin\left(\rho_0-\frac{2\pi}{3}\right) & \sin\left(\rho_0-\frac{4\pi}{3}\right) \\ \cos(\rho_0) & \cos\left(\rho_0-\frac{2\pi}{3}\right) & \cos\left(\rho_0-\frac{4\pi}{3}\right) \end{bmatrix} \times W \begin{bmatrix} \sin(\rho_0) & \cos(\rho_0) \\ \sin\left(\rho_0-\frac{2\pi}{3}\right) & \cos\left(\rho_0-\frac{2\pi}{3}\right) \\ \sin\left(\rho_0-\frac{4\pi}{3}\right) & \cos\left(\rho_0-\frac{4\pi}{3}\right) \end{bmatrix}, \quad (29)$$

$$B2c_{load} = \begin{bmatrix} I_{lq0} \\ -I_{ld0} \end{bmatrix}$$

$$B3c_{load} = \frac{2}{L_l'+6L_{tr}}\frac{2}{3} *$$

$$\left(\begin{bmatrix} \cos(\rho_0) & \cos\left(\rho_0-\frac{2\pi}{3}\right) & \cos\left(\rho_0-\frac{4\pi}{3}\right) \\ -\sin(\rho_0) & -\sin\left(\rho_0-\frac{2\pi}{3}\right) & -\sin\left(\rho_0-\frac{4\pi}{3}\right) \end{bmatrix} W \begin{bmatrix} \sin(\rho_0) & \cos(\rho_0) \\ \sin\left(\rho_0-\frac{2\pi}{3}\right) & \cos\left(\rho_0-\frac{2\pi}{3}\right) \\ \sin\left(\rho_0-\frac{4\pi}{3}\right) & \cos\left(\rho_0-\frac{4\pi}{3}\right) \end{bmatrix} + \begin{bmatrix} \sin(\rho_0) & \sin\left(\rho_0-\frac{2\pi}{3}\right) & \sin\left(\rho_0-\frac{4\pi}{3}\right) \\ \cos(\rho_0) & \cos\left(\rho_0-\frac{2\pi}{3}\right) & \cos\left(\rho_0-\frac{4\pi}{3}\right) \end{bmatrix} W \begin{bmatrix} \cos(\rho_0) & -\sin(\rho_0) \\ \cos\left(\rho_0-\frac{2\pi}{3}\right) & -\sin\left(\rho_0-\frac{2\pi}{3}\right) \\ \cos\left(\rho_0-\frac{4\pi}{3}\right) & -\sin\left(\rho_0-\frac{4\pi}{3}\right) \end{bmatrix} \right) [V_{odq0}]$$

$$W = \begin{bmatrix} 1 & -1 & 0 \\ -2 & 2 & 0 \\ 1 & -1 & 0 \end{bmatrix} \quad for \begin{cases} 0 < \rho < \frac{\pi}{3} \\ \pi < \rho < \frac{4\pi}{3} \end{cases},$$

$$W = \begin{bmatrix} 2 & 0 & -2 \\ -1 & 0 & 1 \\ -1 & 0 & 1 \end{bmatrix} \quad for \begin{cases} \frac{\pi}{3} < \rho < \frac{2\pi}{3} \\ \frac{4\pi}{3} < \rho < \frac{5\pi}{3} \end{cases},$$

$$W = \begin{bmatrix} 0 & 1 & -1 \\ 0 & 1 & -1 \\ 0 & -2 & 2 \end{bmatrix} \quad for \begin{cases} \frac{2\pi}{3} < \rho < \pi \\ \frac{5\pi}{3} < \rho < 2\pi \end{cases}.$$

3-7- Verification of Load Models

Mathematical load models which were previously established in this paper for one-phase RL load as an unbalanced load given by (20) and rectifier load as a nonlinear load given by (26) - (28), are simulated with MATLAB software, and the results are compared with PSCAD/EMTDC software simulation results which are obtained using simulation based on the default blocks. Fig. 6 shows the compared results for dq components of load currents. In this comparison, until t=0.05 s, the load is disconnected from the source and the current loads are zero. At t=0.05 s, the load is connected and draws current. As can be seen, the established models have suitable accuracy.

3-8- General Load Model

For the four types of loads that were modeled in the previous section, a general model is produced with the difference of 30).

$$\begin{aligned} \left[\Delta\tilde{\boldsymbol{x}}_{mload}(k+1)\right] &= Am_{load}\left[\Delta\tilde{\boldsymbol{x}}_{mload}(k)\right] + \\ & B1m_{load}\left[\Delta\tilde{v}_{odq}(k)\right] + B2m_{load}\Delta\tilde{\omega}(k) + \\ & B3m_{load}\Delta\tilde{\rho}(k) + B4m_{load}\Delta\tilde{T}_m(k) \\ \left[\Delta\tilde{i}_{ldq}(k)\right] &= Cm_{load}\left[\Delta\tilde{\boldsymbol{x}}_{mload}(k)\right] \end{aligned} \tag{30}$$

In (30), $B3m_{load}$ and/or $B4m_{load}$ may be zero for some loads. This general model will be used in establishing the state-space model of the overall system.

3-9- DG System Mathematical Model

Due to Fig. 1(b) and equations (6), (11), (14) and (30), state-space equations of DG system will be as (31). This system has twelve state variables. If the load is a three-phase induction motor, the numbers of state variables are increased up to fifteen.

$$\begin{aligned} \left[\tilde{\boldsymbol{X}}_{sys}(k+1)\right] &= Am_{sys}\left[\tilde{\boldsymbol{X}}_{sys}(k)\right] + \\ & B1m_{sys}\begin{bmatrix}\tilde{v}_{odref}(k)\\ \tilde{\omega}_{ref}(k)\end{bmatrix} + B2m_{sys}\left[\Delta\tilde{T}_m(k)\right]; \\ \tilde{\boldsymbol{X}}_{sys}(k) &= \begin{bmatrix} \Delta\tilde{\boldsymbol{x}}_{mLC}(k) \\ \tilde{v}_{odq}(k) \\ \Delta\tilde{\boldsymbol{x}}_{mPLL}(k) \\ \tilde{\omega}(k) \\ \Delta\tilde{\boldsymbol{x}}_{mload}(k) \\ \end{bmatrix} \end{aligned} \tag{31}$$

$$Am_{sys} = \begin{bmatrix} Am_{LC} - B1m_{LC}K & -B1m_{LC}K_{yv} & (B2m_{LC} - B1m_{LC}K_{yvq}K_{\omega})C\omega m_{PLL} & -B1m_{LC}K_{yvq}K_{\omega} & (B3m_{LC} - B1m_{LC}K_d)Cm_{load} \\ Cm_{LC}Am_{LC} - Cm_{LC}B1m_{LC}K & I_{2\times2} - Cm_{LC}B1m_{LC}K_{yv} & Cm_{LC}(B2m_{LC} - B1m_{LC}K_{yvq}K_{\omega})C\omega m_{PLL} & -Cm_{LC}B1m_{LC}K_{yvq}K_{\omega} & Cm_{LC}(B3m_{LC} - B1m_{LC}K_d)Cm_{load} \\ [0_{3\times2} \quad Bm_{PLL}] & 0_{3\times2} & Am_{PLL} & 0_{3\times1} & 0_{3\times(2or5)} \\ C\omega m_{PLL}Bm_{PLL}Cm_{LC} & 0_{1\times2} & C\omega m_{PLL}Am_{PLL} & 1 & 0_{1\times(2or5)} \\ [0_{(2or5)\times2} \quad B1m_{load}] & 0_{(2or5)\times2} & B2m_{load}C\omega m_{PLL} + B3m_{load}C\rho m_{PLL} & 0_{(2or5)\times1} & Am_{load} \end{bmatrix}$$

$$B1m_{sys} = \begin{bmatrix} B1m_{LC}\begin{bmatrix} K_{yvd} & K_{yvd}K_{\omega} \end{bmatrix} \\ Cm_{LC}B1m_{LC}\begin{bmatrix} K_{yvd} & K_{yvd}K_{\omega} \end{bmatrix} \\ 0_{3\times2} \\ 0_{1\times2} \\ 0_{(2or5)\times2} \end{bmatrix}, B2m_{sys} = \begin{bmatrix} 0_{4\times1} \\ 0_{2\times1} \\ 0_{3\times1} \\ 0_{1\times1} \\ B4m_{load} \end{bmatrix}$$

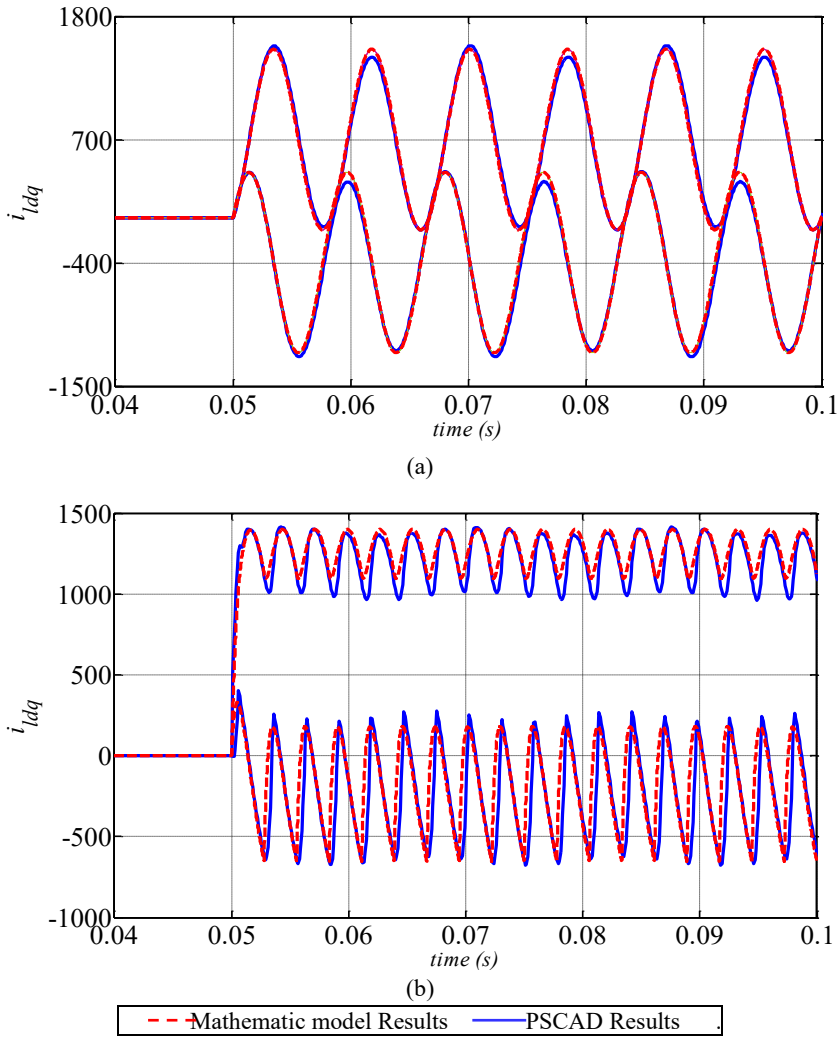

Fig. 6. Compared results for dq components of load currents for four types of loads: (a) one-phase RL load as an unbalanced load (b) rectifier load as a nonlinear load

Table 2. Percentage of THD, load voltage and current unbalance under different control schemes

		$\%THD$	$\%\frac{v_{on}}{v_{op}}$	$\%\frac{i_{on}}{i_{op}}$
Fed-forwarded MPC	RL load (phase a to g)	1.2	0.34	77.9
	RL load (phase a to b)	1.3	0.28	95.4
	Rectifier load	5.0	-	-
	Induction motor load	1.5	0	55.0
Conventional MPC	RL load (phase a to g)	1.3	6.30	79.4
	RL load (phase a to b)	1.4	5.60	96.3
	Rectifier load	8.9	-	-
	Induction motor load	1.5	0.15	55.0
PI–based Controller	RL load (phase a to g)	4.7	2.10	78.7
	RL load (phase a to b)	58.6	31.10	97.4
	Rectifier load	18.4	-	-
	Induction motor load	1.6	0.15	55.0

4- Simulation Results

In this section, the control scheme is applied to a 3 MVA inverter-based DG system and its performance is investigated under various challenging loads. To verify the efficiency of the fed-forwarded MPC, the results are compared with the results under conventional MPC and PI-based controller [3]. Conventional MPC is same as the controller proposed in [4], except that the disturbance signals have been removed and the feed forward signals are not used. The parameters of the DG and loads are given in Table A.1 in the appendix. The detailed switched model of the system is simulated using MATLAB/SIMULINK.

The loads include: (a) two one-phase loads as unbalanced loads, (b) a rectifier load as a nonlinear load and (c) an induction motor load. It is assumed that v_{odref} = 500 V and ω_{ref} = 377 rad/s, but in case (a) and (b), v_{odref} decreases to 400 V during 0.05 seconds. In all cases, the load is initially disconnected until t=0.05 second, then is suddenly connected as a disturbance. In figures, voltages are expressed in Volt and currents in Amper. For all the case studies, percentage of THD, load voltage and current unbalance under different control schemes are represented in Table 2.

4-1- One-phase Loads as an Unbalanced Load

As in Fig. 3(a) shown, a one-phase RL load is connected to the secondary winding of Δ/Y three-phase transformer as an unbalanced load. Fig. 7, Fig. 8 and Fig. 9 show the simulation results for this load under fed-forwarded MPC, Conventional MPC and PI-based controller. As these figures represent, until the load connection, each of the controllers has desired performance, but when the load is connected Conventional MPC and PI-based controller cannot regulate the load voltage and v_{od} begins to oscillation. Due to Table 2, the load current unbalance is above %77, but with using fed-forwarded MPC, load voltage unbalance is % 0.34, while under other schemes this value is above % 2. The value of THD is low under all schemes. However, because of the inability of the controller to regulate v_{oq}, amounts of the harmonic appear in the load voltage for PI-based. At t=0.1 sec v_{odref} decreases to 400 V, and v_{od} tracks it properly under all schemes.

The other loading is a one-phase RL load that is connected between phase a and b without transformer. As Fig. 10, Fig. 11 and Fig. 12, and Table 2 represent, the profiles of the voltages are desired and remain balance with % 0.28 unbalancing in load voltage under fed-forward MPC despite to unbalancing in the load currents where is above % 95. THD of the load voltage under PI-based controller is a high value and it is due to the inability of the controller in regulating of the v_{oq} as mentioned above. Performance of the conventional MPC is better than the PI-based controller under this case study.

4-2- Three-phase Rectifier Load

As shown in Fig. 3(b), a rectifier RL load is connected to secondary winding of Δ/Y three-phase transformer as a nonlinear load. As Fig. 13 shows, the profile of the voltage under fed-forwarded MPC is desired (due to Table 2, THD= % 5) despite to large amount of harmonics in load currents. As Fig. 14 and Fig. 15 show, two other schemes are not able to reduce voltage THD such as fed-forwarded MPC where load voltage has % 8.9 and % 18.4 amount of THD under

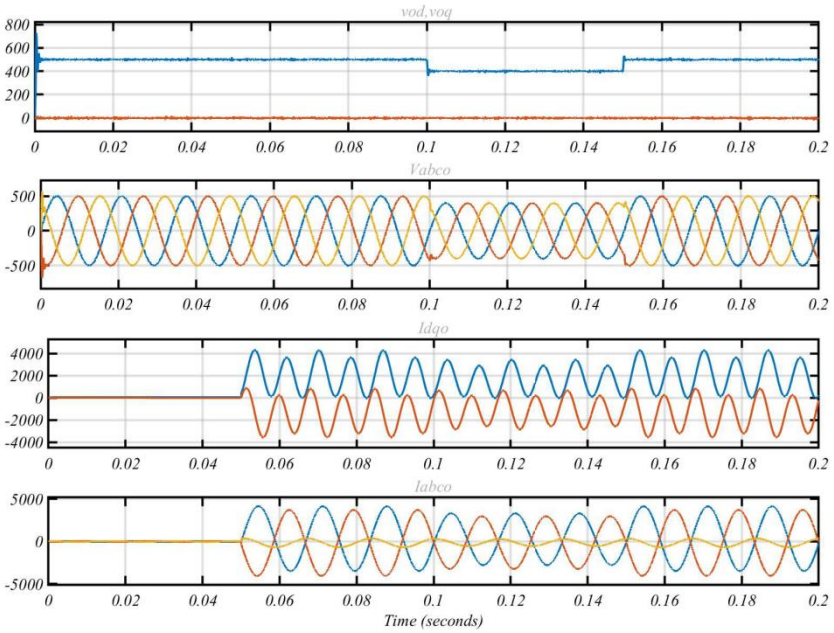

Fig. 7. Simulation results of one-phase RL load connected to secondary winding of Δ/Y three-phase transformer as an unbalanced load under fed-forwarded MPC.

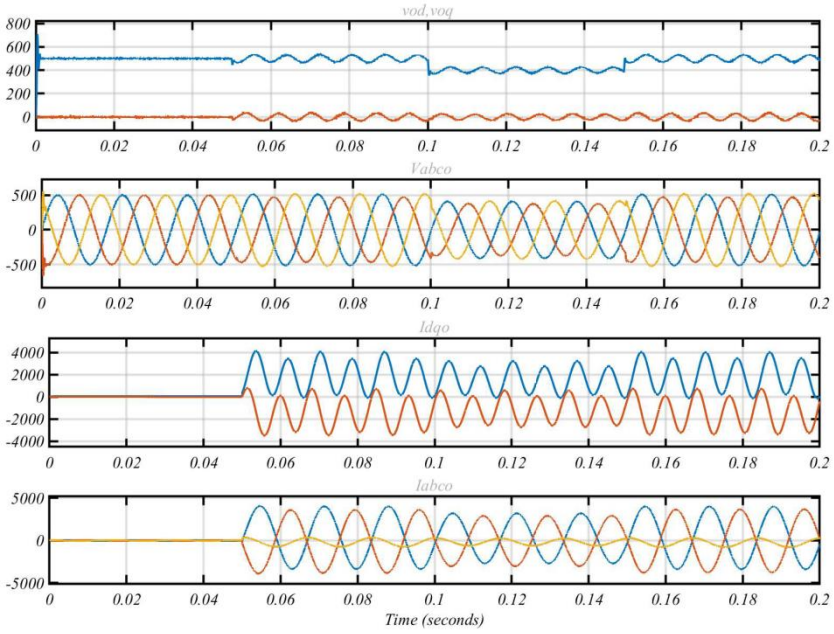

Fig. 8. Simulation results of one-phase RL load connected to secondary winding of Δ/Y three-phase transformer as an unbalanced load under Conventional MPC.

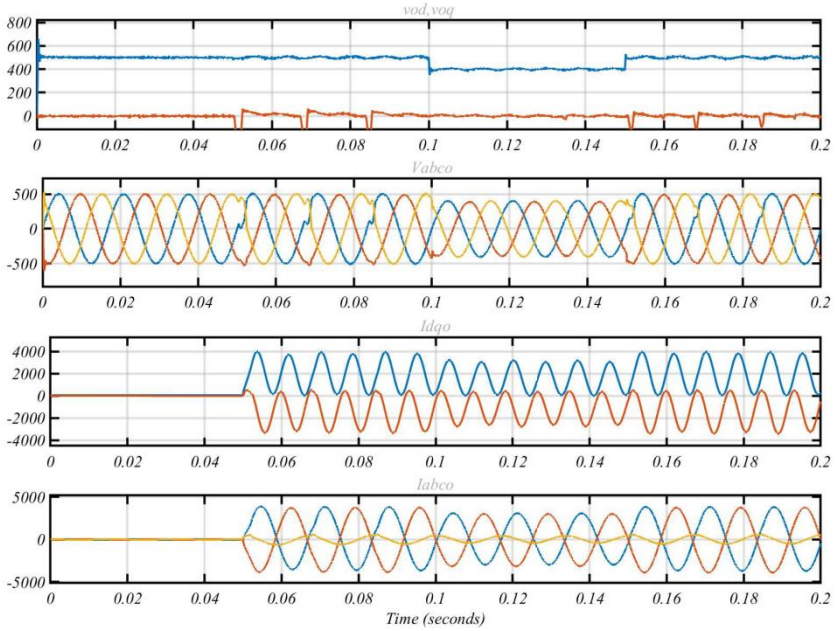

Fig. 9. Simulation results of one-phase RL load connected to secondary winding of Δ/Y three-phase transformer as an unbalanced load under PI-based controller.

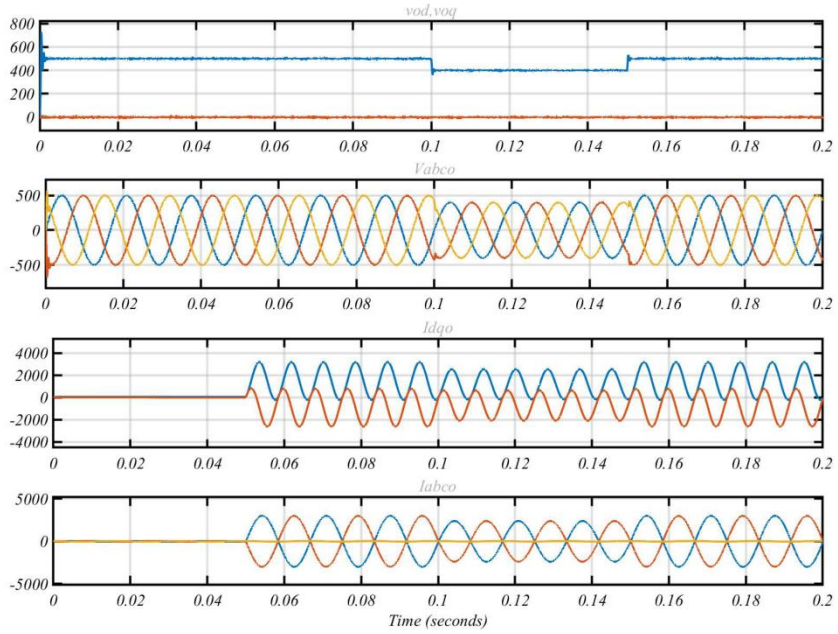

Fig. 10. Simulation results of one-phase RL load connected between phase a and b as an unbalanced load under fed-forwarded MPC.

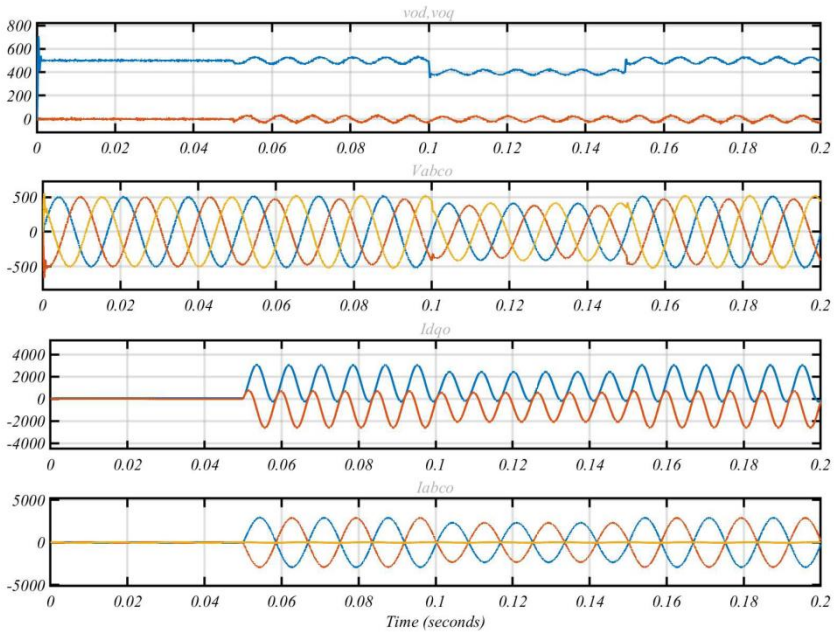

Fig. 11. Simulation results of one-phase RL load connected between phase a and b as an unbalanced load under conventional MPC.

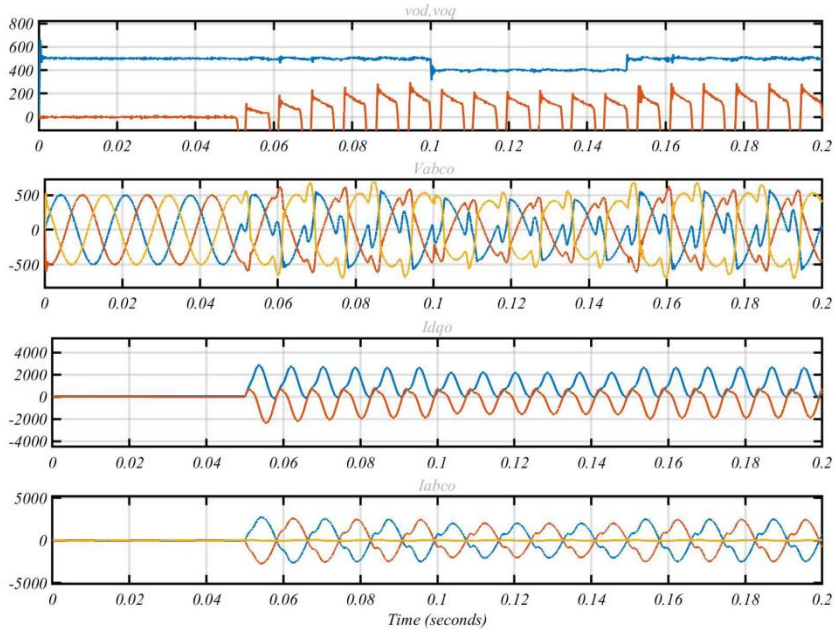

Fig. 12. Simulation results of one-phase RL load connected between phase a and b as an unbalanced load under PI-base controller.

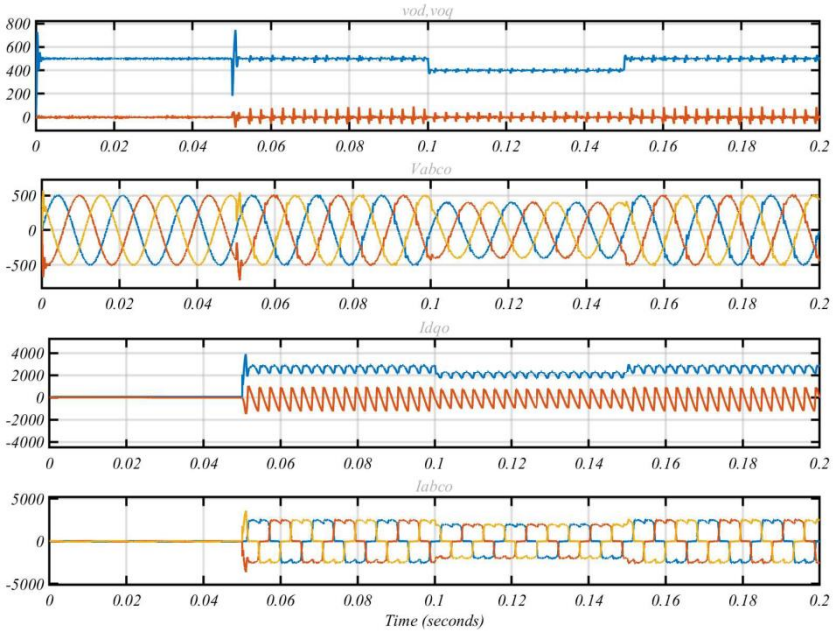

Fig. 13. Simulation results of rectifier RL load is connected to secondary winding of Δ/Y three-phase transformer as a nonlinear load under fed-forwarded MPC.

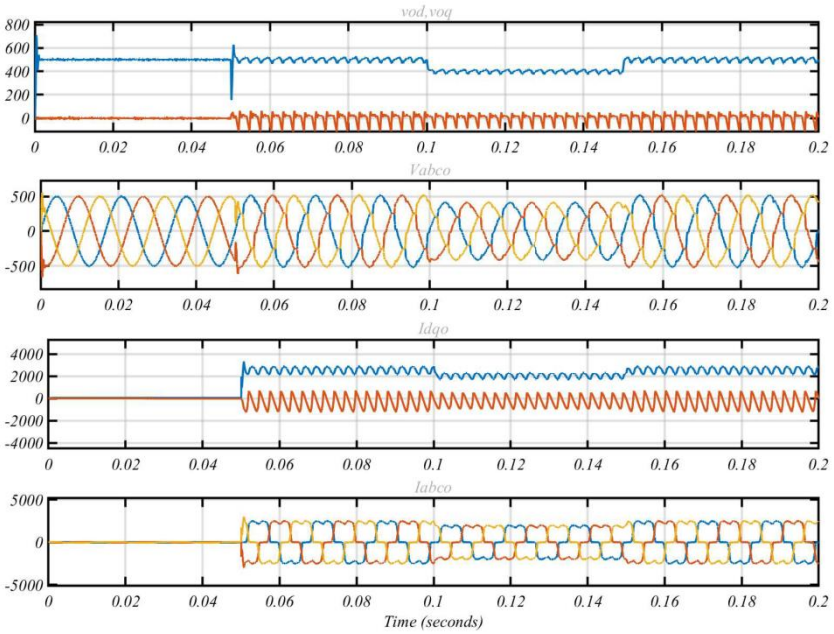

Fig. 14. Simulation results of rectifier RL load is connected to secondary winding of Δ/Y three-phase transformer as a nonlinear load under Conventional MPC.

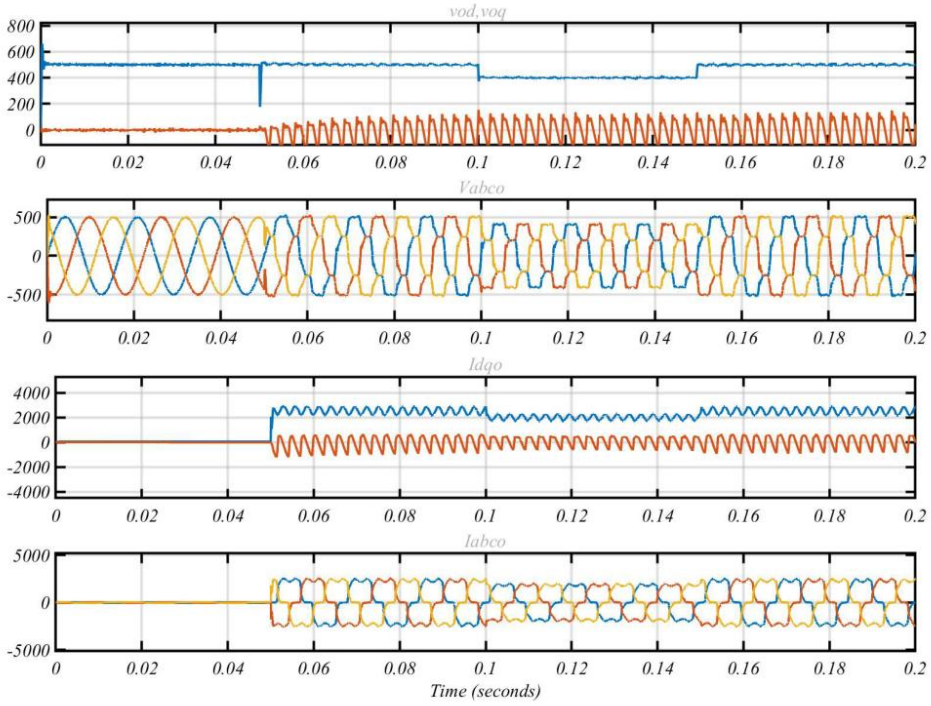

Fig. 15. Simulation results of rectifier RL load is connected to secondary winding of Δ/Y three-phase transformer as a nonlinear load under PI-based controller.

conventional MPC and PI-based controller.

4-3- Induction Motor Load

Fig. 16 depicts the simulation results for induction motor loading under three control schemes. In this case study, all the controllers show the same performance. The reference of v_{od} does not decrease and remains 500 V. As this figure and Table 2 represent, the unbalancing of the motor currents is severe but the voltages are balanced.

5- Stability and Sensitivity Analysis and Robustness Assessment

Based on state-space model of DG system which established in previous section, stability and sensitivity analyses are performed n this section. First, for better analysis representation, discrete-time state-space equations (31) transferred to continuous-time domain and later the eigen-values trajectories will be drawn for a range of load parameters in S-plane. Second, right and left eigen-vectors and p_{ki} are calculated using (32).

$$p_{ki} = v_{ki} w_{ki} \tag{32}$$

In general, $p_{ki} = a + bi$ is a complex number. However, here the relative participation of a state-variable in a mode is of prime interest and therefore, $p_{ki} = \sqrt{a^2 + b^2}$ is reported in tables rather than p_{ki}. In addition, the values are rounded off to the thousandth place and any relative participation smaller than 0.001 is denoted by "0" in the tables.

Since the mathematical models were linearized to a typical operational point, five of them as (33) shows are chosen in this section and control scheme performance is evaluated for them.

$$Q_0 = \begin{bmatrix} I_{d0} \\ I_{q0} \\ V_{od0} \\ V_{oq0} \\ \omega_0 \\ \rho_0 \\ I_{ld0} \\ I_{lq0} \\ \psi_{sd0} \\ \psi_{sq0} \\ \psi_{rd0} \\ \psi_{rq0} \\ \omega_{r0} \end{bmatrix} = \begin{bmatrix} 0 \\ 94.25 \\ 500 \\ 0 \\ 377 \\ 3.1102 \\ 0 \\ 0 \\ 0 \\ 0 \\ 0 \\ 0 \\ 0 \end{bmatrix}, \begin{bmatrix} 0 \\ 60 \\ 300 \\ 0 \\ 400 \\ 2.7785 \\ 0 \\ 0 \\ 0 \\ 0 \\ 0 \\ 0 \\ 0 \end{bmatrix}, \begin{bmatrix} 2516 \\ -1602 \\ 300 \\ 0 \\ 400 \\ 5.2780 \\ 2516 \\ -1662 \\ 0 \\ 0 \\ 0 \\ 0 \\ 0 \end{bmatrix}, \begin{bmatrix} 4341 \\ -2608 \\ 500 \\ 0 \\ 377 \\ 5.2667 \\ 2516 \\ -2702 \\ 0 \\ 0 \\ 0 \\ 0 \\ 0 \end{bmatrix}, \begin{bmatrix} 668 \\ -159 \\ 500 \\ 0 \\ 377 \\ 0.9971 \\ 668 \\ -253 \\ 0.0135 \\ -1.297 \\ -0.061 \\ -1.276 \\ 371 \end{bmatrix} \tag{33}$$

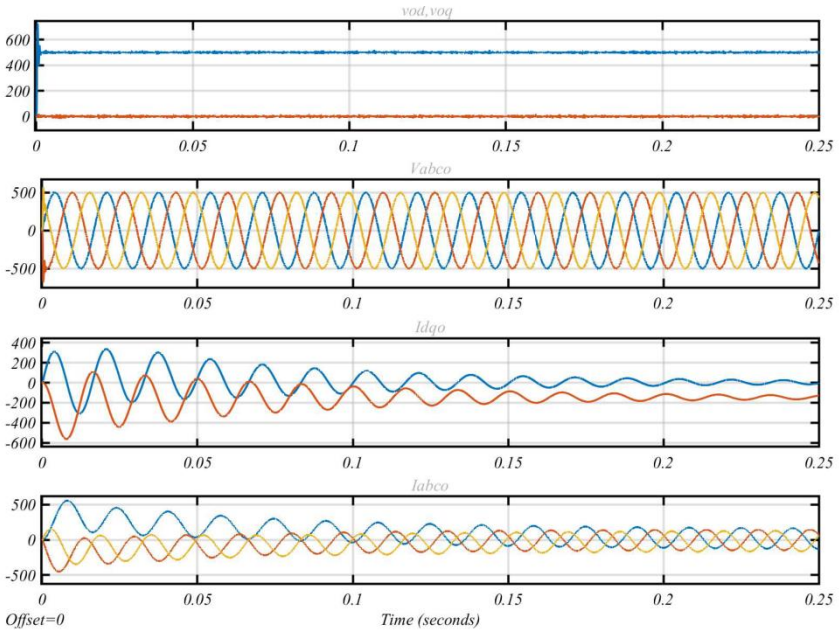

Fig. 16. Simulation results of induction motor load under three control schemes.

Table 3. Relative participations of PLL states

	λ_{1PLL}=-2e5	λ_{2PLL}=-887	λ_{3PLL}=-113	λ_{4PLL}=0
$\tilde{x}_{1PLL}$	1.145	0.145	0	0
$\tilde{x}_{2PLL}$	0.145	1.145	0	0
$\tilde{\rho}$	0	0	1	0
$\tilde{\omega}$	0	0	0	1

The results are approximately the same for these operational points and the results of one have been presented.

First, stability and sensitivity analysis for four types of loads are considered and then robustness of the controller is evaluated against uncertainties in LC filter parameters (i.e. R_f, L_f and C_f).

5-1- Stability and Sensitivity Analysis

For all types of loads, PLL has stable eigen-values λ_{1PLL}=-2e5, λ_{2PLL}=-887, λ_{3PLL}=-113 and λ_{4PLL}=0 which are not affected by the LC filter and load parameters. Integrator in PLL which produces ρ from ω causes zero eigen-value. Additionlly, PLL state variables do not affect other eigen-values. Relative participations of PLL states are presented in Table 3. The eigen-values and relative participation factors of system with three-phase balanced RL load are presented in Table 4. Eigen-values are at the left-side of the S-plane and are divided into four modes where all are oscillatory. Mode 1 is seriously affected by the inverter output currents. Output voltages of LC filter (load voltages) have the most effect on mode 2 and 3. Load currents affect mode 4. Fig. 16 shows the comparison between dominant eigen-values of a system with and without a controller for this load. In this figure, three types of loads (three-phase RL balanced, one-phase RL unbalanced and three-phase induction motor load) are considered. For each load type, two sub-figure are represented which the first is eigen-values positions with specified given parameters and the second is eigen-value trajectory under variation of one parameter of that load when it is supplied by the VSC with and without using fed-forwarded MPC controller in S-plane. Variable parameter is resistant to the load, except induction motor load which is nominal KVA for it. As can be seen in Fig. 16 (a), the controller causes the modes 2 and 3 which seriously affected the load voltages move far from imaginary axis. Additionally, this matter is also true for mode 4. Based on the equation $\xi = cos(\angle\lambda)$, the smaller angle of λ relative to left-side of real axis causes the larger damping ratio. Due to Fig. 16 (a), system eigen-values with a controller have larger damping ratio. Fig. 16 (b) shows trajectory of mode 2 and 3 which the positive imaginary parts of them have been shown for more clarity. The sensitivity of these modes relative to load changing ($L_l = 137[\mu H]$, $10[m\Omega] \le R_1 \le 2[\Omega]$) i.e. $\frac{\partial \lambda_{3,5}}{\partial |Z_l|}$, for system with a controller is less than without a controller.

The eigen-values and relative participation factors of the one-phase RL load as an unbalanced load are presented in

Table 4. Eigen-values and relative participation factors of system with three-phase balanced RL load

		$\lambda_{1,2}$= -35355 ± 370i	$\lambda_{3,4}$= -3620 ± 9946i	$\lambda_{5,6}$= -3598 ±9521i	$\lambda_{7,8}$= -622 ± 390i
	mode	1	2	3	4
states	*LC filter*	0.576	0.076	0.075	0.001
		0.576	0.076	0.075	0.001
		0.109	0.322	0.309	0
		0.109	0.322	0.309	0
		0.042	0.282	0.292	0.015
		0.042	0.282	0.292	0.015
	Load	0.009	0.017	0.015	0.516
		0.009	0.017	0.015	0.516

Table 5. Eigen-values and relative participation factors of system with one-phase RL load as an unbalanced load

		$\lambda_{1,2}$= -36023 ±293 i	$\lambda_{3,4}$= -3360 ±10089i	$\lambda_{5,6}$= -3363 ± 9625i	$\lambda_{7,8}$= -670 ±381i
	mode	1	2	3	4
states	*LC filter*	0.603	0.091	0.073	0
		0.611	0.074	0.086	0
		0.102	0.348	0.275	0
		0.108	0.290	0.337	0
		0.041	0.301	0.258	0.001
		0.043	0.249	0.315	0.005
	Load	0	0.001	0.001	0.500
		0.003	0.004	0.005	0.505

Table 5. In this load, participations are approximately the same as the balanced RL load. Fig. 17 shows comparison between the dominant eigen-values of the system for this load with and without a controller. As can be seen in Fig. 17 (c), a system without a controller has two eigen-values at the right-side of the imaginary axis which cause instability of the system. The controller causes the modes 2 and 3 which are affected by the load voltages and move far from imaginary axis. Additionally, this matter is true for mode 4. Due to Fig. 17 (c), system eigen-values with a controller have a larger damping ratio. Fig. 17 (d) shows trajectory of mode 2 and 3 where their sensitivity is relative to load changing ($L_l = 21.8[\mu H]$, $5[m\Omega] \le R_1 \le 0.5[\Omega]$) i.e. $\frac{\partial \lambda_{3,5}}{\partial |Z_l|}$, for a system with a controller is less than without a controller.

In Table 6, eigen-values of a system with three-phase induction motor load have been presented. Oscillatory modes which are seriously affected by the state variables of load (linkage fluxes of rotor and stator and rotational speed of shaft) are modes 4 and 5. These modes have slow dynamic due to huge inductance of stator and rotor. Mode 5 is very close to the imaginary axis, but fortunately its sensitivity is relative to VA of motor i.e. $\frac{\partial \lambda_{9,10}}{\partial |S_m|}$, is very low and approximately zero. Mode 6 which is a non-oscillatory mode is the closest eigen-value to the imaginary axis and is completely dependent on mechanical state variable of motor i.e. rotational speed of shaft which has a very slow dynamic. Fig. 17(e) shows the comparison of dominant eigen-values of system with and without a controller for this load. Fig. 17(f) shows trajectory of mode 2 and 3 when S_m increases from 100 KVA to 1500 KVA.

Table 6. Eigen-values and relative participation factors of system with three-phase induction motor load

		$\lambda_{1,2}$= -35175 ±367i	$\lambda_{3,4}$= -3700 ±9926i	$\lambda_{5,6}$= -3667 ±9498i	$\lambda_{7,8}$= -275 ±391i	$\lambda_{9,10}$= -0.759 ±377i	λ_{11}= -0.052
	mode	1	2	3	4	5	6
states	*LC filter*	0.581	0.076	0.074	0.001	0	0
		0.581	0.076	0.074	0.001	0	0
		0.113	0.324	0.311	0	0	0
		0.113	0.324	0.311	0	0	0
		0.043	0.285	0.295	0.017	0	0
		0.043	0.285	0.295	0.017	0	0
	Load	0.011	0.021	0.018	0.308	0.209	0
		0.011	0.021	0.018	0.308	0.209	0
		0	0	0	0.209	0.29	0
		0	0	0	0.209	0.29	0
		0	0	0	0	0	1

Table 7. Eigen-values and relative participation factors of system with rectifier load as a nonlinear load

		λ_1= -35268	λ_2= -36207	$\lambda_{3,4}$= -3439 ±10042i	$\lambda_{5,6}$= -3451 ±9514i	$\lambda_{7,8}$= -2982 ±423i
	mode	1	2	3	4	5
states	*LC filter*	1.08	0.076	0.056	0.106	0.008
		0.086	1.026	0.121	0.055	0
		0.212	0.007	0.251	0.453	0.001
		0.014	0.175	0.458	0.232	0
		0.08	0.004	0.215	0.432	0.03
		0.006	0.071	0.401	0.222	0
	Load	0.02	0.001	0.013	0.025	0.538
		0.005	0.005	0.008	0.007	0.507

Eigen-values and relative participations of a system with a rectifier load are presented in Table 7 and Fig. 18 shows the comparison of dominant eigen-values of a system with and a without controller for rectifier load. As can be seen from this figure, the system under heavy load is unstable if the controller is not used, but with employing the controller stability of system will increase.

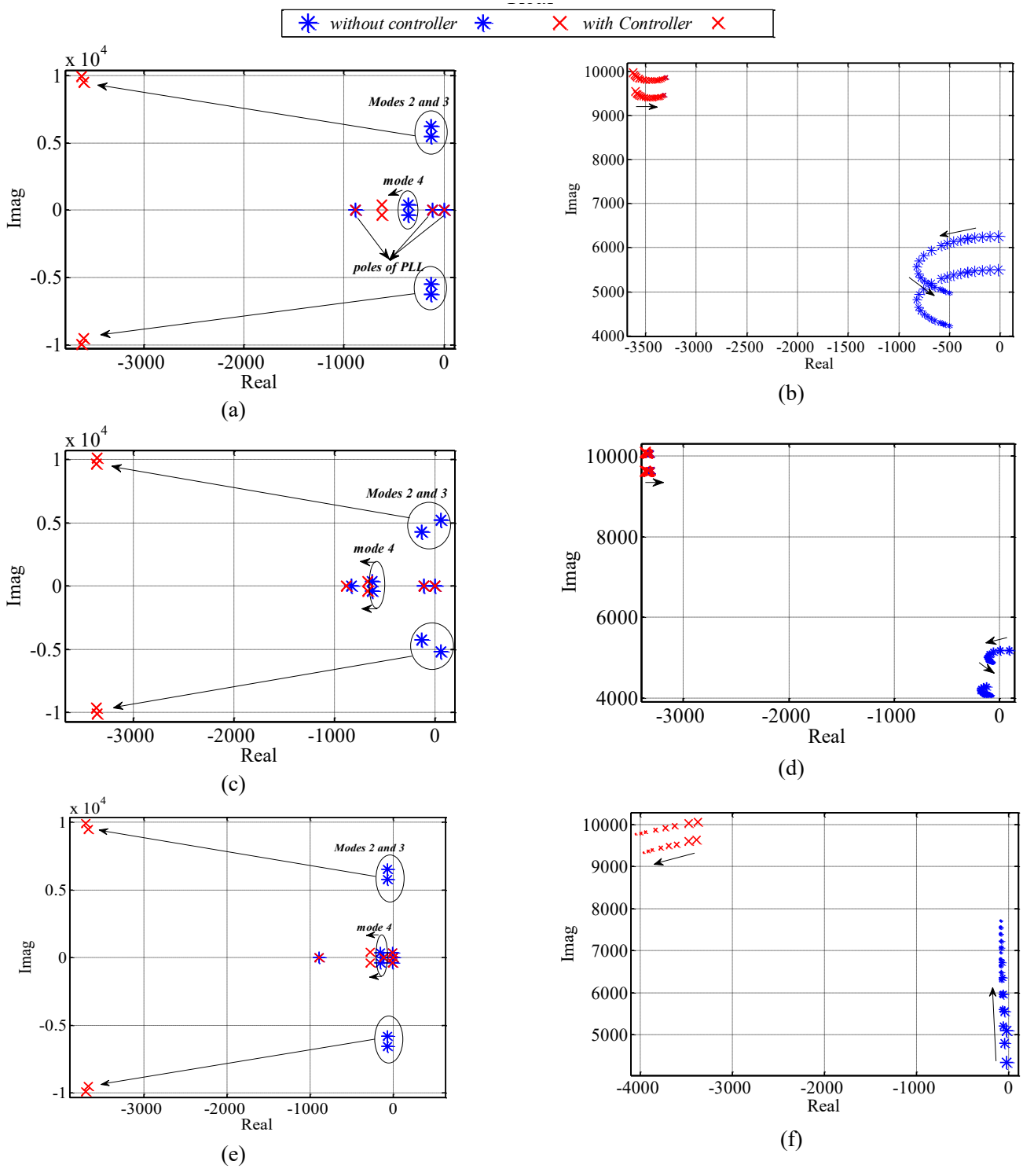

Fig. 17. Comparison between dominant eigen-values of system with and without fed-forwarded MPC controller when load is:

(I) three-phase balanced RL load (a) L_l=137 [μH] ,R_l=83 [mΩ] (b) L_l=137 [μH],10 [mΩ]≤R_l≤2[Ω]

(II)one-phase RL load as an unbalanced load (c) L_l=21.8 [μH] , R_l=17 [mΩ] (d) L_l=21.8 [μH],5 [mΩ]≤R_l≤0.5[Ω]

(III) three-phase induction motor (e) S_m=800[KVA] (f) 100 [KVA]≤S_m≤1500[KVA]

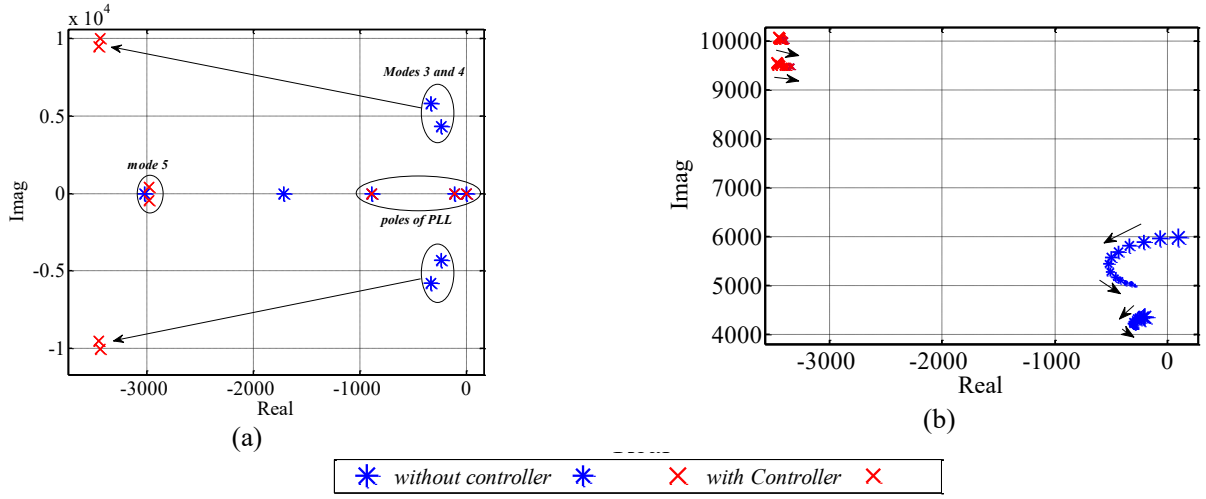

Fig. 18. Comparison between dominant eigen-values of system with and without fed-forwarded MPC controller when load is rectifier load as a nonlinear load (a) L_l=20 [μH] , R_l=0.7 [Ω] (b) L_l=20 [μH] , 100 [mΩ]≤R_l≤3[Ω].

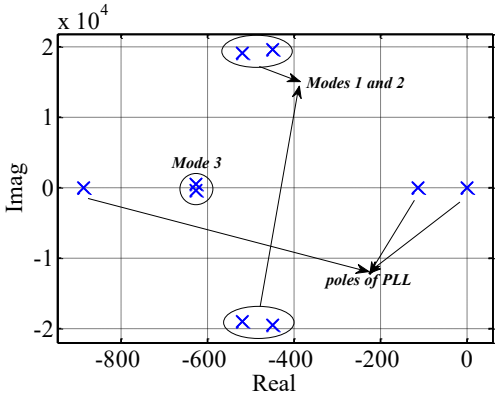

Fig. 19. Rout loci of the eigen-values under uncertainties on LC filter parameters ($3R_f$,$3L_f$,$0.3C_f$)

5-2- Robustness assessment

To assess the robustness of the control scheme, -70% mismatch for L_f and +300% mismatch for R_f and L_f are assumed and the rout loci of the eigen-values is drawn. As depicted in Fig. 19, the result shows a stable performance of the control scheme under the assumed uncertainties, but the speed of the responses decrease and oscillation increases.

6- Experimental Results

As shown in Fig 20, a 1.5 KVA three-phase inverter-based DG is implemented to verify the proposed control scheme. The parameters of the experimental setup are listed in Table A.2 in appendix. Output of a variable three-phase AC power supply is rectified and filtered with a DC capacitors to provide V_{DC}. A dual-core processor F28M35H52C1 based on DSP and ARM cores is used as the digital controller. Six SKM 200GB125D high-speed insulated gate bipolar transistors (IGBTs) are used for implementing the inverter. Hcpl316j ICs are used to drive the IGBTs. Since the PWM signals are produced by the digital processor and the its CPU clock is 150 MHz, the frequency switching is set to 9375 Hz and is close to 10 KHz which is used in simulation studies. Voltage sensors are used to sense phase to ground voltages of the LC filter capacitors. Current sensors are used to sense inverter currents and the load currents are calculated in the processor based on KCL law $i_{load}=i_{inverter}-i_{capacitor}$ where capacitor current can be calculated based on its measured voltage i.e.

$i_c = C_f \frac{v_o(k)-v_o(k-1)}{T_s}$. To measure the load current with the

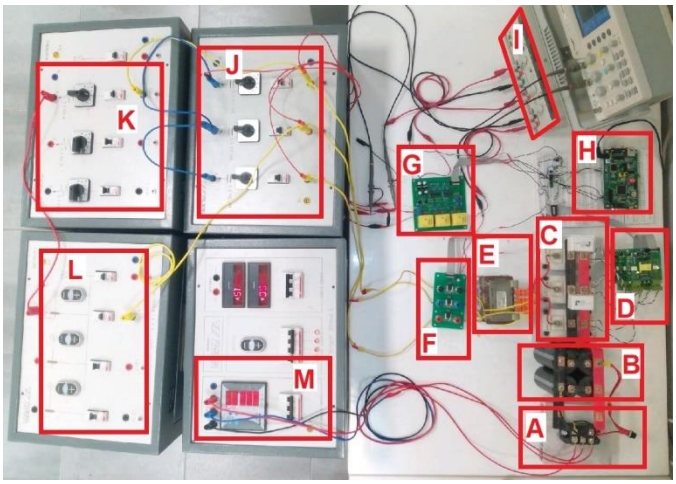

Fig. 20. Experimental setup of the implemented DG system. A: three-phase rectifier, B: DC capacitor, C: three-phase inverter, D: IGBT's gate drivers, E: inductors of the LC filter, F: current sensors module, G: voltage sensors module, H: DSP board as controller, I: DC power supply of the boards, J: capacitors of the LC filter, K: resistor loads, L: inductor loads, M: variable three-phase AC power supply.

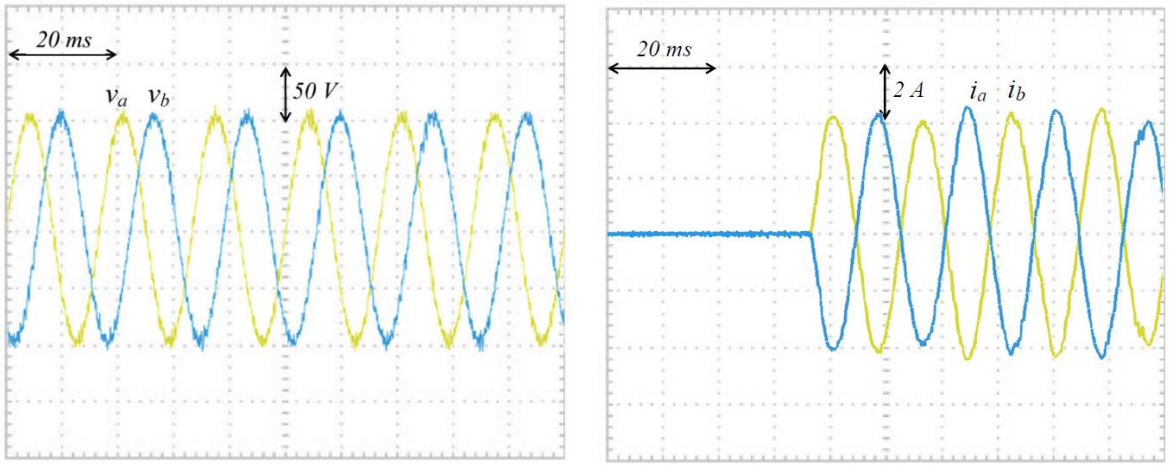

(a) (b)

Fig. 21. One-phase load connected between phase a and b as the unbalanced load (a) phase to ground load voltages of a and b phases (b) load currents of phase a and b.

oscilloscope, three 1 Ohm and high power resistors are used in series with the load where are not shown in Fig. 20.

To consider the performance of the control scheme two load types are used in the experimental section: (a) one-phase load connected between phase a and b without 3-phase transformer as the unbalanced load and (b) rectifier load as the nonlinear load. In these studies, v_{odref} = 100 V and ω_{ref} = 377 rad/s.

6-1- One-phase Load Connected Between Phase a and b Without 3-phase Transformer as the Unbalanced Load

Fig. 21 shows the phase to ground voltages and currents of the load. As the results show, when the unbalanced load is suddenly connected, the load voltages profile remain balanced and without any transient distortion. Since the RL load is connected between phase a and b, currents of these phases have 180 degrees phase difference with each other. The peak of the voltages is about 100 V which is equal to v_{odref} and the RMS value is about 70 V. RMS of the currents is 2.82 A.

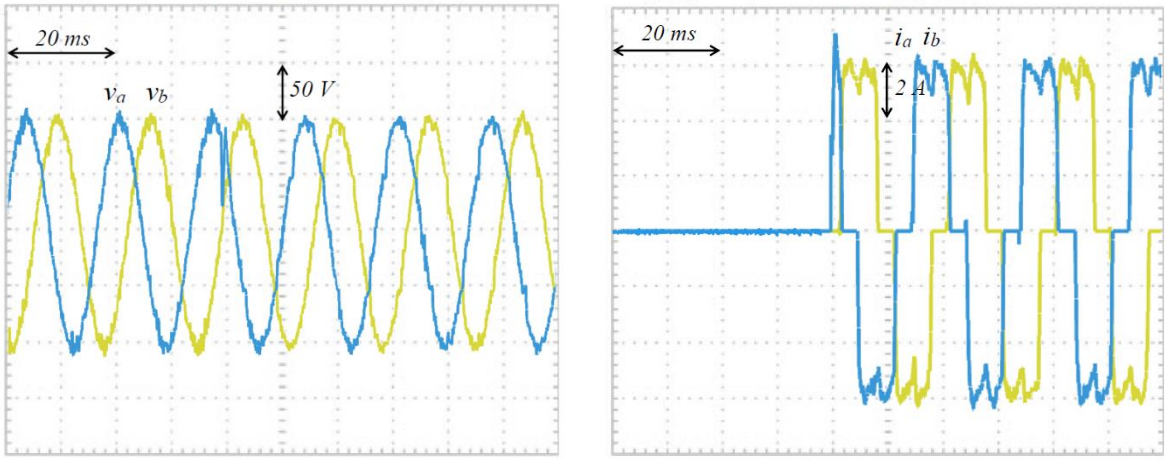

(a) (b)

Fig. 22. Rectifier load as the nonlinear load (a) phase to ground load voltages of a and b phases (b) load currents of phase a and b.

6-2- Rectifier Load as the Nonlinear Load

Fig. 22 shows the phase of the ground voltages and currents of the load. This figure shows when this nonlinear load is suddenly connected. Despite the large amount of current harmonics, the load voltages are not extremely distorted. The peak of the voltages is about 100 V which is equal to v_{odref} and RMS value of the currents is about 4 A.

7- Conclusions

This paper presents a small-signal stability analysis of an individual DG system controlled by MPC with feed-forwarded load currents as disturbances where its load may be one of the four types of three-phase balanced RL load, one-phase RL load as an unbalanced load, three-phase induction motor load and rectifier load as a nonlinear load. Established analysis based on the mathematical models which were produced the show system under its control scheme will be stable for a range of load parameter variances. Additionally, robustness of the controller was assessed under a large range of LC filter parameters uncertainties and has shown that the DG system remains stable under these large uncertainties but its stability decreases. additionally, the suitable performance of the control scheme is illustrated by the simulation and experimental studies. In simulation studies critical load i.e. unbalanced, rectifier and motoring loads and in the experimental studies unbalanced and rectifier loads have been considered.

8- Nomenclature

v	Output voltage of VSC
i	Output current of VSC
v_o	PCC voltage
i_o	Load current (PCC output current)
m	Modulating index
V_{DC}	VSC DC-link voltage
L_f	Filter inductance
C_f	Filter capacitance
R_f	Sum of filter resistance and switches on-state resistance
L_l	Load inductance
R_l	Load resistance
L_{tr}	Transformer inductance (from primary side)
L_l'	Load inductance transferred to the primary side
R_l'	Load resistance transferred to the primary side
a	Transformer turn ratio
T_m	Mechanical load torque
w_{ki}	kth element of right eigen-vector of λ_i
v_{ki}	kth element of left eigen-vector of λ_i
p_{ki}	Participation of kth state in ith eigen-value
Greek symbols	
ω	VSC AC-side Frequency
ρ	dq reference frame angle.
ψ_s	Linkage flux of stator
ψ_r	Linkage flux of rotor
ω_r	Rotational speed of rotor
ξ	Damping ratio
$\Delta(\cdot)$	Denoting the difference of a variable
λ_i	ith eigen-value
Subscript	
$_{abc}$	abc components of $(\cdot)$
$_{dq}$	dq components of $(\cdot)$
$_c$	Subscript denoting the continues-time value of a coefficient
$_m$	Subscript denoting the discrete-time value of a coefficient
$_0$	Subscript denoting the steady-state value of a variable
Superscript	
$\tilde{}$	Superscript denoting small-signal perturbation of a variable

References

[1] Chowdhury, S., et al. (2009). Microgrids and Active Distribution Networks. IET Press.

[2] Yazdani, A. and Dash, P. P. (2009). "A Control Methodology and Characterization of Dynamics for a Photovoltaic (PV) System Interfaced with a Distribution Network. " IEEE Transactions on Power Delivery 24(3): 1538–1551.

[3] Delghavi, M. B. and Yazdani, A. (2009). "A control strategy for islanded operation of a distributed resource (DR) unit. " IEEE Power Eng. Soc. Gen. Meeting: 1–8.

[4] Saleh, A., et al. (2019). "Model Predictive Control of Distributed Generations with Feed-forward Output Currents, " IEEE Transactions on Smart Grid 10(2): 1488–1500.

[5] Jin, T., et al. (2019). "Model Predictive Voltage Control Based on Finite Control Set With Computation Time Delay Compensation for PV Systems. " IEEE Transactions on Energy Conversion 34(1): 330–338.

[6] Hamzeh, M., et al. (2015). "Robust Control of an Islanded Microgrid under Unbalanced and Nonlinear Load Conditions. " IEEE Journal of Emerging and Selected Topics in Power Electronics.

[7] Lascu, C. (2020). "Sliding Mode Direct Voltage Control of Voltage Source Converters with LC Filters for Pulsed Power Loads. " IEEE Transactions On Industrial Electronics.

[8] Delghavi, M. B., et al. (2016). " Fractional-Order Sliding-Mode Control of Islanded Distributed Energy Resource Systems. " IEEE Trans. Sustainable Energy.

[9] Kabalan, M., et al. (2016). "Large Signal Lyapunov-Based Stability Studies in Microgrids: A Review. " IEEE Trans. Smart Grid.

[10] Yang, C., et al. (2020). "Placing Grid-Forming Converters to Enhance Small Signal Stability of PLL-Integrated Power Systems. " IEEE Transaction on Power System.

[11] Bottrell, N., et al. (2013). "Dynamic stability of amicrogrid with an active load. " IEEE Transaction on Power Electronics 28(11): 5107–5119.

[12] Kahrobaeian, A. and Mohamed, Y. A.-R. I. (2014). "Analysis and mitigation of low-frequency instabilities in autonomous medium-voltage converter based microgrids with dynamic loads. " IEEE Transaction on Industrial Electronic 61(4): 1643–1658.

[13] Zheng, H., et al. (2020). "Large-Signal Stability Analysis for VSC-HVDC Systems Based on Mixed Potential Theory. " IEEE Transactions on Power Delivery 3(4): 1939 – 1948.

[14] Xie, W., et al. (2021). "System-Level Large-Signal Stability Analysis of Droop-Controlled DC Microgrids. " IEEE Transactions on Power Electronics 36(4): 4224-436.

[15] Krause, P. C., et al. (2002). Analysis of Electric Machinery and Drive Systems, IEEE Press.

[16] Katiraei, F., et al. (2005). "Micro-grid autonomous operation during and subsequent to islanding process. " IEEE Transaction on Power Delivery 20(1): 248–257.

[17] Peng, Y., et al. (2019). "Modeling and Stability Analysis of Inverter-based Microgrid under Harmonic Conditions. " IEEE Transactions on Smart Grid.

[18] Shuai, Z., et al. (2019). "Transient Response Analysis of Inverter-Based Microgrids Under Unbalanced Conditions Using a Dynamic Phasor Model." IEEE Transactions on Industrial Electronics 66(4): 2868-2879.

[19] Aderibole, A., et al. (2018). "A Critical Assessment of Oscillatory Modes in Multi-Microgrids Comprising of Synchronous and Inverter Based Distributed Generation. " IEEE Transactions on Smart Grid.

[20] Nandanoori, S. P., et al. (2020). "Distributed Small-Signal Stability Conditions for Inverter-Based Unbalanced Microgrids. " IEEE Transactions On Power Systems 35(5).

[21] Delghavi, M. B. and Yazdani, A. (2012). "A Unified Control Strategy for Electronically Interfaced Distributed Energy Resources. " IEEE Transactions on Power Delivery 27(2): 803-812.

[22] Saleh, A. and Deihimi, A. (2018). "Model Predictive Control of Distributed Energy Resources with Predictive Set-Points for Grid-Connected Operation. " AUT Journal of Electrical Engineering 50(2): 3-14.

[23] Wang, L. (2009). Model Predictive Control System Design and Implementation Using MATLAB, London.

[24] Zheng, C., et al. (2020). "Current-Sensorless Finite-Set Model Predictive Control for LC-Filtered Voltage Source Inverters. " IEEE Transactions on Power Electronics 35(1): 1086-1095.

[25] Zeng, Z., et al. (2011). "Study on small signal stability of microgrids: A review and a new approach. " Renewable and Sustainable Energy Reviews 15: 4818–4828.

[26] Mahdavi, M. S., et al. (2019). "Frequency Regulation of AUT Microgrid Using Modified Fuzzy PI Controller for Flywheel Energy Storage System. " AUT Journal of Electrical Engineering 51(1): 31-38.

[27] Rahmani, R. and Fakharian, A. (2018). "A Distributed Control Architecture for Autonomous Operation of a Hybrid AC/DC Microgrid System. " AUT Journal of Electrical Engineering 50(1): 25-32.

[28] Rokrok, E., et al. (2020). "A Robust Control Strategy for Distributed Generations in Islanded Microgrids." AUT Journal of Electrical Engineering, 52(1): 107-120.

9- Appendix

Table A.1. Parameter of the DG and loads in simulation Studies.

Parameter	Value	Remark	
L_f	100 µH		Converter and LC filter
C_f	500 µF		
R	1.5 mΩ		
V_{DC}	1600 V		
f_s	10 KHz	Switching frequency	
T_s	10 µs	Sampling time	MPC
R_1	0.249 Ω		Unbalanced Load (between phase *a* and *b*)
L_1	411 µH		
R_2	8.3 mΩ		Unbalanced Load (phase *a* to ground)
L_2	13.7 µH		
Tr2	1173/208 V_{rms}	Trans. X= 0.1 pu	
R_3	0.35 Ω		rectifier Load
L_3	10 µH		
Tr3	600/600 V_{rms}	Trans. X= 0.1 pu	
S_m	110 KVA	Rated power	Induction Motor Load
V_m	400 V	Rated voltage	
ω	377 rad/s	Rated frequency	
R_r	625.8 mΩ =	R_r referred to stator	
R_s	44.34 mΩ =	Stator resistance	
L_m	8.831 mH =	Magnetizing inductance	
L_{lr}	5.473 mH =	L_{lr} referred to stator	
L_{ls}	0.2341 mH =	stator leakage	

Table A.2. Parameter of the DG and loads in experimental Studies.

Parameter	Value	Remark	
Lf	1.4 mH		Converter and LC filter
Cf	40 µF		
VDC	400 V		
fs	9375 Hz	Switching frequency	
Ts	20 µs	Sampling time	MPC
R1	16.6 Ω		Unbalanced Load (between phase *a* and *b*)
L1	109.6 mH		
R_2	28 Ω		Nonlinear Load
L_2	0.8 mH		

HOW TO CITE THIS ARTICLE

A.H. Saleh, Modeling, Small-Signal Stability Analyzing and Implementing of an Inverter-based Distributed Generation with Feed-forwarded Model Predictive Controller , AUT J. Elec. Eng., 53(2) (2021) 261-286.

DOI: 10.22060/eej.2021.19696.5405